Reprinted from:

Perspectives in Fluid Dynamics

A Collective Introduction to Current Research

Edited by

G. K. Batchelor

H. K. Moffatt

M. G. Worster

© Cambridge University Press 2000

Contents

8

Solidification of Fluids

M. G. WORSTER

1 Introduction

It is a matter of common experience that liquids become solid when cooled sufficiently. Rain falls as hail or snow when the weather is cold, frozen ponds can be walked upon, toffee becomes hard and brittle when removed from the heated pan, and hot lava flowing destructively over the landscape cools to form a new passive terrain of solid rock. Moreover, the production of solids from liquids has been important technologically since the earliest ages of mankind, as tools, weapons and ornaments began to be fashioned from bronze, iron and gold. And as we enter the 21st century, the production and processing of materials from melts has increasing prominence, for example in the growth of large, single crystals for the fabrication of semiconductor wafers and in the casting of high-performance turbine blades for the aerospace industry.

Solidification, the transformation of liquid into solid, requires the removal of heat, first to cool the liquid to its freezing temperature, then to effect the transformation itself. Because heat can be carried by a flowing liquid, we can appreciate immediately that fluid mechanics plays a significant role in the solidification of fluids.

But this is only part of the interest that solidification can hold for fluid dynamicists. The dynamical behaviour of fluids is determined by the forces that act on them and the geometry of the domains in which they flow. The cooling associated with solidification creates density gradients and hence buoyancy forces that can drive convection of the liquid being solidified. At the same time, the interface between solid and liquid forms a free boundary that deforms in response to the heat transferred to it and hence responds to the flow. Indeed, in many circumstances the interface is unstable, prone to form corrugations that can develop into the sort of branched structures typical of snowflakes.

This is particularly true when the liquid is not pure. When a second component is dissolved in the liquid, the solid that forms usually has a different composition than the liquid (ice grown from salt water is almost pure), and the rejected component must be transported away from the solidification front. Such transport is enhanced near protrusions of the solid into the liquid, which therefore grow more rapidly; the interface is *unstable*. Fluid flow influences this transport, and there have been many attempts to use fluid flow to control the morphology of the phase boundary.

A consequence of these instabilities can be the formation of a *mushy region*, a region in which the solid–liquid interface has become so convoluted that the solid forms a matrix of crystals bathed in the remaining liquid. From a macroscopic, fluid-mechanical point of view, the mushy layer is a porous medium. It is a reactive porous medium because continued solidification of the solid matrix or, indeed, its dissolution changes its permeability. In many solidification problems of practical interest it is necessary to solve the equations of fluid motion in a liquid region and couple that flow with the flow calculated in a neighbouring mushy region. It is the intimate coupling of fluid mechanics, heat and mass transfer in different media and the determination of the free boundaries between them that makes solidification such a rich and fascinating subject for fluid dynamicists.

2 Some fundamentals of solidification

2.1 The Stefan condition

During solidification, randomly moving liquid molecules become attached and incorporated into the crystalline lattice of the solid. Their loss of entropy results in the liberation of heat which must be transported away if solidification is to proceed. If the local rate of solidification is V_n (see figure 1) then the rate of release of latent heat per unit area is $\rho_s L V_n$ where ρ_s is the density of the solid and L is the latent heat per unit mass. Conservation of heat requires that this be balanced by the net heat flux away from the interface, which gives us the Stefan condition

$$\rho_s L V_n = \boldsymbol{n} \cdot \boldsymbol{q}_l - \boldsymbol{n} \cdot \boldsymbol{q}_s, \tag{2.1}$$

where $\boldsymbol{q}$ is the local heat flux vector, $\boldsymbol{n}$ is a unit normal pointing into the liquid and subscripts s and l refer to properties of the solid and liquid respectively. Throughout the solid, heat transfer is by conduction alone and

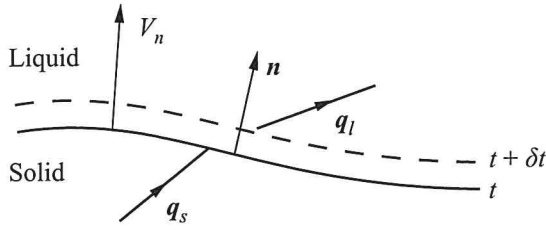$$\boldsymbol{q}_s = -k_s \nabla T, \tag{2.2}$$

Figure 1. Schematic diagram of the local heat balance at a solidification front. The latent heat released per unit area in time δt is $\rho_s V_n L \delta t$ while the heat transported away is $(\boldsymbol{n} \cdot \boldsymbol{q}_l - \boldsymbol{n} \cdot \boldsymbol{q}_s) \delta t$.

where k is the thermal conductivity and T is the temperature field. In the liquid, heat transfer may be enhanced by convection. Though $\boldsymbol{q}_l$ is given by an expression similar to (2.2) at the solidification front, often the convective heat flux is parameterized and we shall leave equation (2.1) in its general form for the time being.

2.2 Two simple Stefan problems

As a simple illustration of the role of latent heat, consider the solidification from a cooled boundary of a pure melt initially at its equilibrium freezing temperature T_m (figure 2a). For simplicity, in this section, the material properties of the solid and liquid phases are assumed to be equal, and the defining subscripts are omitted. Solid occupies the region $0 < z < h(t)$, the boundary $z = 0$ is maintained at temperature $T_B < T_m$ and the solid–liquid interface is assumed to be at temperature T_m. The temperature field in the solid satisfies the diffusion equation

$$\frac{\partial T}{\partial t} = \kappa \frac{\partial^2 T}{\partial z^2} , \tag{2.3}$$

where $\kappa = k/\rho C_p$ is the thermal diffusivity of the solid and C_p is its specific heat capacity, and boundary conditions

$$T = T_B \quad (z = 0), \qquad T = T_m \quad (z = h(t)). \tag{2.4a, b}$$

The moving position of the solid–liquid interface $h(t)$ is determined by heat conservation as expressed by equation (2.1), which can be written

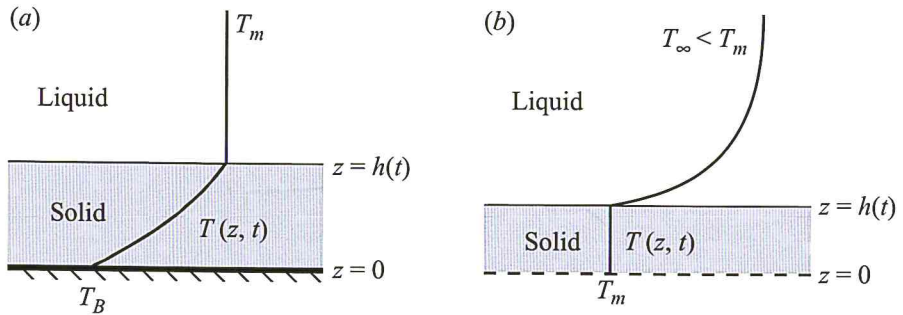$$\rho L \dot{h} = k \frac{\partial T}{\partial z} \bigg|_{z=h-} . \tag{2.5}$$

Figure 2. (a) Solidification of a melt from a cooled boundary at $z = 0$. The latent heat is conducted back through the solid to the boundary. (b) In contrast, when a crystal nucleates and grows into a supercooled melt, the latent heat is conducted into the liquid. Here, the line $z = 0$ is a symmetry plane of the one-dimensional crystal.

Equations (2.3)–(2.5) admit a similarity solution

$$T - T_B = (T_m - T_B)\frac{\mathrm{erf}\,\eta}{\mathrm{erf}\,\lambda}, \qquad h(t) = 2\lambda\sqrt{\kappa t}, \qquad (2.6a, b)$$

where

$$\mathrm{erf}\,x \equiv \frac{2}{\sqrt{\pi}} \int_0^x \mathrm{e}^{-u^2}\mathrm{d}u$$

is the error function and

$$\eta = \frac{z}{2\sqrt{\kappa t}} \qquad (2.7)$$

is a similarity variable. The coefficient λ, which is a measure of the solidification rate, satisfies the transcendental equation

$$G(\lambda) \equiv \sqrt{\pi}\lambda\mathrm{e}^{\lambda^2}\mathrm{erf}\,\lambda = S^{-1}, \qquad (2.8)$$

where the Stefan number

$$S = \frac{L}{C_p(T_m - T_B)} \qquad (2.9)$$

is the ratio of the latent heat of solidification to the sensible heat required to cool the newly formed solid to the boundary temperature. The solution to equation (2.8) is displayed in figure 3(a). We see that λ decreases as S increases; the solidification rate is slow when the latent heat is large.

A useful approximation can be made when the Stefan number is large. Because the solidification rate is then small, the temperature field in the solid
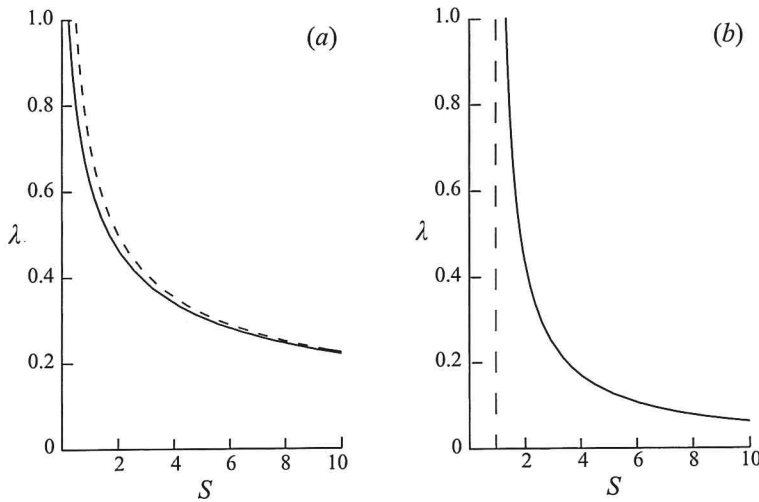
Figure 3. The scaled growth rates λ as functions of the Stefan number S predicted from the models illustrated in figure 2. The dashed curve in (a) is the result of the quasi-stationary model. The asymptote in (b) is at $S = 1$.

region is quasi-steady, hence linear, and the Stefan condition (2.5) can be approximated by

$$\rho L \dot{h} \simeq k \frac{(T_m - T_B)}{h}. \qquad (2.10)$$

This equation is readily solved to give

$$h \simeq \sqrt{\frac{2\kappa t}{S}}, \quad \text{i.e.} \quad \lambda \simeq \frac{1}{\sqrt{2S}}. \qquad (2.11)$$

The dashed curve in figure 3(a) shows that this gives a good approximation, with less than 7% relative error for $S > 2$.

A similar, one-dimensional solution can be found when the liquid is initially supercooled with temperature $T_\infty < T_m$. In this case (depicted in figure 2b), the solid is isothermal, with temperature T_m, the temperature in the liquid satisfies the diffusion equation (2.3), and the Stefan condition gives

$$\rho L \dot{h} = -k \frac{\partial T}{\partial z}\bigg|_{z=h+}. \qquad (2.12)$$

There is again a similarity solution

$$T - T_\infty = (T_m - T_\infty)\frac{\text{erfc}\,\eta}{\text{erfc}\,\lambda}, \qquad h = 2\lambda\sqrt{\kappa t} \qquad (2.13)$$

with, now,

$$F(\lambda) \equiv \sqrt{\pi}\lambda e^{\lambda^2} \operatorname{erfc}\lambda = S^{-1}, \qquad \text{where} \qquad S = \frac{L}{C_p(T_m - T_\infty)} \qquad (2.14)$$

and the complementary error function $\operatorname{erfc}x \equiv 1 - \operatorname{erf}x$.

The solution for λ is displayed in figure 3(b), where we see that no solution exists for $S < 1$. It is certainly possible to devise an experiment with $S < 1$ so the question remains: what happens in this case and why is the present mathematical formulation inadequate?

2.3 Kinetic undercooling

The problem lies in the assumption that the solid–liquid interface has temperature T_m. The freezing temperature T_m is an equilibrium temperature at which solid and liquid can coexist without change of phase. For solidification to proceed, the phase boundary must have a temperature below T_m, which is found to be related to the rate of solidification. The simplest case, appropriate to interfaces that are molecularly rough (unfacetted), is that

$$V_n = \mathscr{G}(T_m - T), \qquad (2.15)$$

where the kinetic coefficient $\mathscr{G}$ is constant (Kirkpatrick 1975). With this new boundary condition replacing (2.4b), there is no closed-form solution of the equations for general values of the Stefan number but it is straightforward to show that

$$h \sim \mathscr{G}(T_m - T_\infty)t, \qquad t \ll 1. \qquad (2.16)$$

Further, it can be shown that

$$h \sim 2\lambda\sqrt{\kappa t} \quad \text{as} \quad t \to \infty \quad \text{when} \quad S > 1 \qquad (2.17)$$

and that

$$h \sim (1 - S)\mathscr{G}(T_m - T_\infty)t \quad \text{as} \quad t \to \infty \quad \text{when} \quad S < 1 \qquad (2.18)$$

(Umantsev 1985). Kinetic undercooling gives a finite solidification rate at time zero, solidification rates remain finite for all time, and the similarity solution is recovered asymptotically where it exists ($S > 1$). In general terms we can say that when $S > 1$ the rate of solidification is controlled by the rate of removal of latent heat, while for $S < 1$ the kinetics of molecular attachment is rate controlling.

In the first case described above, of solidification from a cooled boundary, kinetics plays a minor role, simply regularizing the solution at early times.

We shall see later, however, that kinetics can play a major role when coupled with convection of the liquid.

2.4 The Gibbs–Thomson effect

Solidification is intrinsically concerned with interfaces, and one of the fundamental properties of interfaces is that intermolecular forces acting between the materials either side of them result in a surface energy. This manifests itself at a fluid–fluid interface as a surface tension, which creates a pressure jump across the interface when it is curved (see Chapter 1). The pressure variations generated at a corrugated fluid–fluid interface drive flows in both fluids that tend to restore the interface to a planar state. Excess surface energy associated with a corrugated solid–melt interface similarly drives the interface towards a planar state but the mechanism is different. Although there is a pressure jump across a curved solid–melt interface, it is taken up by elastic stresses in the solid and does not drive any flow. However, the same intermolecular forces that give rise to surface tension change the phase equilibria causing, in particular, the equilibrium freezing temperature to be depressed when the interface is convex towards the liquid (at a crest). This is expressed mathematically by the Gibbs–Thomson relationship

$$T_e = T_m - \Gamma \nabla \cdot \mathbf{n}, \tag{2.19}$$

where T_e is the equilibrium freezing temperature, $\mathbf{n}$ is the normal to the interface pointing into the liquid, $\Gamma = \gamma T_m / \rho_s L$, and γ is the surface energy. Note that $\nabla \cdot \mathbf{n}$ is the curvature of the interface. Thus heat flows from troughs to crests, promoting solidification at the troughs and melting at the crests, and the interface is driven towards a planar state.

2.5 Morphological instability

The ideas of diffusion-limited solidification and surface energy combine in determining the stability of the one-dimensional solutions presented earlier. As a simple illustration of the principal ideas,[1] consider a temperature field given by

$$T(x, z, t) = T_m + Gz + \hat{\theta} e^{i\alpha x - \alpha z + \sigma t} \tag{2.20}$$

[1] The analysis is presented here rather informally but can be derived rigorously from an asymptotic analysis of the full governing equations when the characteristic wavelength of the disturbance is much shorter than the diffusion length, i.e. in the limit $\alpha \gg \Delta T / G = V / \kappa$. This can be justified *a posteriori* as shown below.

in the liquid region

$$z > \zeta(x,t) = \hat{\zeta}e^{i\alpha x + \sigma t} \, . \tag{2.21}$$

These represent a sinusoidal perturbation to a planar solid–liquid interface at $z = 0$ in a frame of reference fixed to the undisturbed interface and the corresponding perturbation to the temperature field satisfying the quasi-steady diffusion equation. The perturbation coefficients $\hat{\theta}$ and $\hat{\zeta}$ are related by the Stefan condition and linearized Gibbs–Thomson relationship,

$$\rho L(V + \zeta_t) = -kT_z \quad \text{and} \quad T = T_m + \Gamma\zeta_{xx} \quad (z = \zeta). \tag{2.22a,b}$$

By substituting expressions (2.20) and (2.21) into (2.22), and keeping only those terms that are linear in $\hat{\theta}$ and $\hat{\zeta}$, we obtain

$$\rho L\sigma\hat{\zeta} = k\alpha\hat{\theta} \quad \text{and} \quad \hat{\theta} + G\hat{\zeta} = -\Gamma\alpha^2\hat{\zeta}, \tag{2.23}$$

which combine to give

$$\sigma(\alpha) = \frac{k}{\rho L}\alpha(-G - \Gamma\alpha^2) \, . \tag{2.24}$$

There is a close mathematical analogy between this instability and the Saffman–Taylor instability that occurs when a viscous fluid displaces a more-viscous fluid in a porous medium or Hele-Shaw cell. The dispersion relation (2.24) is identical in form to equation (2.26) of Chapter 2 and is represented by a graph similar to figure 5 of that chapter.

We see that if G is positive (the temperature increases into the liquid) then the growth rate of the perturbations σ is negative; all disturbances decay and the interface is stable. On the other hand, if G is negative then there is a range of wavenumbers $0 < \alpha < \alpha_c \equiv \sqrt{-G/\Gamma}$ in which the growth rate σ is positive. Disturbances with wavenumbers less than α_c (wavelengths greater than $2\pi/\alpha_c$) will grow to form corrugations of the solid–liquid interface: the interface is said to be morphologically unstable.

The instability arises because diffusion of heat between the interface and the liquid is enhanced where the interface protrudes into the liquid, as described in Chapter 2, figure 2, and in a review by Langer (1980). When the liquid is supercooled ($G < 0$), heat is diffused away from the interface into the liquid, preferentially at protrusions, which causes them to grow. Opposing this tendency is the Gibbs–Thomson effect that causes perturbations to a planar interface to decay, as we saw in the previous section.

The competition between these two effects selects a length scale for the most unstable perturbations: diffusion is more rapid on small length scales, which causes σ to increase with α; surface energy acts even more strongly

on smaller length scales, which causes σ ultimately to decrease with α. The maximum growth rate is readily determined from (2.24) to occur at $\alpha = \alpha_c/\sqrt{3}$. This corresponds to a wavelength

$$\lambda \propto \sqrt{\Gamma/(-G)} = \sqrt{l_\Gamma l_T}, \tag{2.25}$$

where $l_T = \Delta T/(-G)$ is a characteristic length scale for temperature variations and $l_\Gamma = \Gamma/\Delta T$ is the so-called capillary length corresponding to an undercooling of ΔT. Typical values of l_T and l_Γ are a few centimetres and a few nanometres respectively, so $l_T \gg l_\Gamma$. Equation (2.25) expresses the rule of thumb that the length scale characteristic of morphological instabilities is the geometric mean of the diffusion length and the capillary length.

In this section we have seen how the rate of solidification of a pure melt is usually constrained by the rate at which latent heat can be transported, since the rate of molecular attachment is usually much faster than thermal transport rates. In consequence, we have seen that when the Stefan number is large, as is true in many practical applications, thermal diffusion fields can be approximated as being quasi-steady. Finally, we have seen that planar solidification fronts are morphologically unstable when the liquid is supercooled. The rest of this chapter will build on these ideas to examine the influence of fluid flow and to study the effects of dissolved solutes.

3 Convective heat transfer

The Stefan condition (2.1) expresses a balance between conductive heat transfer through the solid phase, heat transfer through the melt and the latent heat released at a solidification front. The heat flux carried by the melt is enhanced by fluid motions, which may be forced by external agents (e.g. stirring) or induced by buoyancy forces arising as the melt is cooled prior to being solidified. In this section we shall explore the role of convective heat transfer in determining the rate of solidification.

3.1 Flow near a stagnation point

One of the fundamental flows near a rigid boundary is the flow near a stagnation point, which is a ubiquitous feature of bounded flows and is therefore important to understand in its own right. It is, in addition, convenient for our present purpose since the heat transfer it induces is independent of position parallel to the boundary and so its influence on solidification is one-dimensional.

Consider a solid of uniform temperature T_m growing into a supercooled

melt of temperature $T_\infty < T_m$. Near a two-dimensional stagnation point at the phase boundary, the stream function can be written as

$$\psi = Ex\delta f(z/\delta) \tag{3.1}$$

(Batchelor 1967, pp. 285 ff), where (x, z) are coordinates parallel and normal to the boundary, with origin at the stagnation point, E represents the strength of the (extensional) flow, δ is a length scale normal to the interface and f is a dimensionless function. Throughout this section we shall employ the quasi-stationary approximation that the rate of solidification is slow compared both with the fluid velocities involved and with the rate of heat conduction. The velocity $\boldsymbol{u} = (\psi_z, -\psi_x)$ influences heat transfer via the steady advection–diffusion equation

$$\boldsymbol{u} \cdot \nabla T = \kappa \nabla^2 T. \tag{3.2}$$

We can choose $\delta = \sqrt{\kappa/E}$ to balance the terms representing vertical advection and diffusion of heat, and write

$$T - T_\infty = (T_m - T_\infty) g(z/\delta). \tag{3.3}$$

The dimensionless functions f and g satisfy the ordinary-differential equations

$$Prf''' + ff'' - f'^2 = -1, \qquad g'' + fg' = 0, \tag{3.4a,b}$$

with respect to the single independent variable $\eta = z/\delta$ in which the Prandtl number $Pr = \nu/\kappa$, is the the ratio of the kinematic viscosity ν to the thermal diffusivity κ. These equations are subject to the boundary conditions

$$f = f' = 0, \quad g = 1 \qquad (\eta = 0), \tag{3.5a–c}$$

$$f' \to 1, \quad g \to 0 \qquad (\eta \to \infty). \tag{3.6a,b}$$

Conditions (3.5a–c) express the facts that there is no flow through the boundary, that there is no slip and that the temperature is fixed, respectively. The far-field conditions (3.6a, b) describe the imposed linear irrotational flow $\mathbf{u} = (Ex, -Ez)$, $\psi = Exz$, and the far-field temperature. Once the equations have been solved (see figure 4), the Stefan condition (2.1) can be used to determine the rate of solidification as

$$V = -\frac{\sqrt{\kappa E}}{S} g'(0). \tag{3.7}$$

Note that $g'(0)$ is negative, so the solidification rate is positive and increases with the strength of the flow E. Note too that the ratio of the vertical
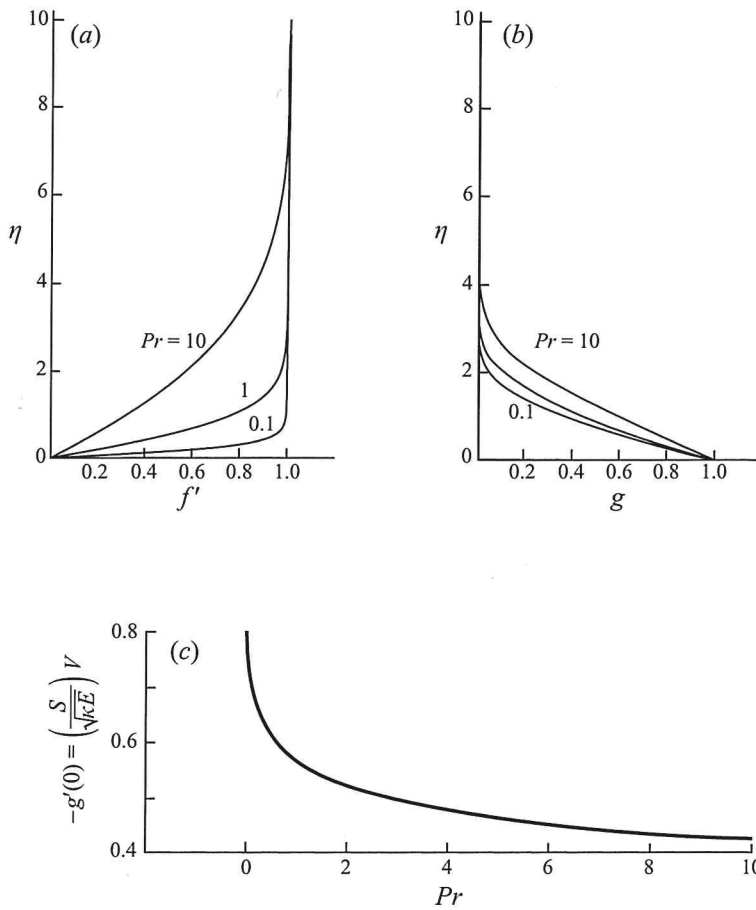
Figure 4. (*a*) The horizontal velocity f' and (*b*) the temperature g as functions of the similarity variable η. Notice the reduction in thickness of the viscous boundary layer relative to the thermal boundary layer as the Prandtl number Pr decreases. (*c*) The dimensionless solidification rate of a one-dimensional crystal growing into a supercooled melt, towards an oncoming stagnation point, as a function of the Prandtl number Pr. The solidification rate $-g'(0) \rightarrow \sqrt{2/\pi} \simeq 0.798$ as $Pr \rightarrow 0$. It decreases as the Prandtl number increases and the influence of the flow diminishes.

velocity, $-\psi_x \sim \sqrt{\kappa E}$, to the solidification rate V is $O(S)$, so the quasi-steady approximation is valid when the Stefan number S is large.

The essential result, that in this case solidification is enhanced by the flow (equation (3.7) shows that $V \propto \sqrt{E}$), can be understood as follows. Since the solid is of uniform temperature T_m, all of the latent heat of solidification must be transported through the melt. The effect of the flow towards the boundary is to diminish the thickness of the thermal boundary layer $\delta = \sqrt{\kappa/E}$, which

steepens the thermal gradients, and increases the rate of heat transfer and, hence, of solidification.

An important dimensionless parameter determining the strength of inter-action between the velocity and thermal fields and hence the strength of interaction between fluid flow and solidification is the Prandtl number *Pr*. In a stagnation-point flow, vorticity is confined to a viscous boundary layer of thickness $\delta_v \sim \sqrt{v/E} = Pr^{1/2}\delta$. Outside the viscous boundary layer the flow is irrotational, $u \simeq (Ex, -Ez)$, and the vertical velocity varies linearly with distance from the boundary. It is inside the viscous boundary layer that the effects of the no-slip condition are felt: the vertical velocity is smaller there, ultimately decreasing quadratically with distance from the boundary as the boundary is approached. Thus when the Prandtl number is large, the thermal boundary layer sits inside the viscous boundary layer and the influence of the flow is weaker than when the Prandtl number is small. In the latter case there is negligible change in temperature across the viscous boundary layer, and the thermal field (and hence the solidification) is controlled by the irrotational flow. It is straightforward then to show that, outside the viscous boundary layer,

$$f \sim \eta, \qquad g \sim \operatorname{erfc}\left(\eta/\sqrt{2}\right) \tag{3.8}$$

so that

$$g'(0) = -\sqrt{\frac{2}{\pi}} \qquad \text{and} \qquad V \sim \frac{1}{S}\sqrt{\frac{2\kappa E}{\pi}}. \tag{3.9}$$

This result is valid for $Pr \ll 1$. Results for a range of Prandtl numbers are displayed in figure 4, showing that indeed the influence of flow diminishes as *Pr* increases, as has also been found for the more complex flow past a needle crystal growing into a supercooled melt (see Xu 1994 for example).

The results of this simple analysis are fundamental to the understanding of the influence of flow on morphological instabilities (§ 5) and the enhancement by flow of the growth of isolated dendrites (see Glicksman & Marsh 1993 for a review).

3.2 Changing balances

When a melt is solidifying against a cooled boundary, all the heat lost from the system is conducted through the solid to the boundary. The Stefan condition (2.1) is best interpreted, in this case, by writing it in the form

$$\hat{n} \cdot q_s = \rho_s L V_n + \hat{n} \cdot q_l, \tag{3.10}$$

where $\hat{n} = -n$ is the unit normal pointing into the solid. Thus, instead of thinking of the rate of solidification being controlled by the mismatch between heat fluxes either side of the interface, we can think of the heat flux through the solid towards the boundary being the sum of the latent heat released and the heat flux from the melt. We shall see that most of the time one or other of these dominates.

As an example, consider a simple model of ice growing on the surface of the ocean. The upper boundary of the ice, in contact with the atmosphere, is assumed to be at fixed temperature T_B, while the ocean is assumed to deliver a constant flux of heat $\hat{n} \cdot q_l = F$ to the underside of the ice. By using the quasi-stationary assumption for the heat flow in the solid, equation (3.10) can be written in dimensionless form as

$$\frac{1}{h} = S\dot{h} + 1, \tag{3.11}$$

where the thickness of the layer h has been scaled with $H \equiv k\Delta T/F$, time has been scaled with H^2/κ and $\Delta T = T_m - T_B$. The full solution of (3.11) for $h(t)$ is given implicitly by

$$\ln\frac{1}{1-h} - h = \frac{t}{S}, \tag{3.12}$$

but the inherent physical balances can most readily be understood in terms of its asymptotic limits. At early times, solidification is rapid, and the release of latent heat overwhelms the heat flux from the ocean. Equation (3.11) can then be approximated by

$$\frac{1}{h} \sim S\dot{h}, \tag{3.13}$$

which has the simple solution $h \sim \sqrt{2t/S}$, as we have seen before. At late times, solidification is slow, latent heat release becomes negligible and there is a balance between the heat flux from the ocean and that conducted back through the solid. Equation (3.11) shows simply that $h \sim 1$ at this stage. In practice, as T_B and F vary diurnally and seasonally, this thermal balance is maintained; the thickness of the ice varies secularly with the changing boundary conditions, little influenced by considerations of latent heat.

In a confined system, such as in a casting or magma chamber, the balance of fluxes can change more than once. Imagine, for example, a rectangular mould which is cooled through its top boundary, while the remaining boundaries are insulated. The melt is initially hotter than its freezing temperature and cools as heat is transferred by thermal convection to the solidification front and thence by conduction to the cold upper boundary. The convective

heat flux from the melt can be approximated by

$$\hat{\boldsymbol{n}} \cdot \boldsymbol{q}_l = \lambda k \left(\frac{\alpha g}{\kappa \nu} \right)^{1/3} (T_l - T_m)^{4/3} \tag{3.14}$$

when the Rayleigh number is large (see Chapter 6), where T_l is the temperature of the melt, α is the coefficient of thermal expansion, g is the acceleration due to gravity and λ is a constant. Equation (3.10) becomes

$$\frac{1}{h} = (S + C\theta)\dot{h} + \mathscr{F}C\theta^{4/3} \tag{3.15}$$

and is augmented by

$$(1 - h)\dot{\theta} = -\mathscr{F}\theta^{4/3}, \tag{3.16}$$

which describes the cooling of the melt (Huppert & Worster 1991). Here, h has been scaled with the initial depth of the melt H, time with H^2/κ, and $\theta = (T_l - T_m)/(T_0 - T_m)$, where T_0 is the initial temperature of the melt. The dimensionless parameters are the Stefan number $S = L/C_p(T_m - T_B)$,

$$C = \frac{T_0 - T_m}{T_m - T_B} \quad \text{and} \quad \mathscr{F} = \lambda \left(\frac{\alpha g (T_0 - T_m) H^3}{\kappa \nu} \right)^{1/3}. \tag{3.17}$$

The additional term $C\theta$ inside the brackets on the right-hand side of (3.15) represents the sensible heat required to cool the melt to its freezing temperature.

Equations (3.15) and (3.16) are subject to the initial conditions

$$h = 0, \qquad \theta = 1 \qquad (t = 0). \tag{3.18}$$

These equations do not have a closed-form solution but can readily be solved numerically. At very early times before the melt has cooled significantly (so $\theta \simeq 1$) the dominant heat balance is between conduction through the solid and latent-heat release,

$$\frac{1}{a} \sim (S + C)\dot{a}, \tag{3.19}$$

leading to the characteristic growth proportional to the square root of time, $h \sim \sqrt{2t/(S + C)}$.

This growth is quickly arrested by the heat flux from the melt and the balance becomes

$$\frac{1}{h} \sim \mathscr{F}C\theta^{4/3} . \tag{3.20}$$

If the temperature of the melt were to remain fixed then there would be no

further growth. But the cooling of the melt, determined by

$$\dot{\theta} \sim -\mathscr{F}\theta^{4/3} \tag{3.21}$$

(an approximation to (3.16) given that h is still small), allows the secular growth of solid, according to (3.20). These approximate equations are readily solved to give

$$\theta \sim \left(1 + \tfrac{1}{3}\mathscr{F}t\right)^{-3}, \qquad h \sim \frac{1}{\mathscr{F}C}\left(1 + \tfrac{1}{3}\mathscr{F}t\right)^{4}, \tag{3.22}$$

from which we see that the rate of solidification actually *increases* with time. Eventually, however, the melt is cooled to a temperature close to T_m, the convective heat flux is diminished and a balance between conduction and latent-heat release is re-established. Since then θ is close to zero, $h \sim \sqrt{2t/S}$, so the continuing growth of solid is faster than it would have been had there been no convection. The overall result is that, though convection retards solidification for a while, ultimately it causes a casting to become completely solidified more quickly, starting from a given initial temperature.

4 Binary alloys

Everything described so far applies strictly only to pure melts: pure water, pure silicon and pure copper, for example. Yet few liquids are actually pure: sea water contains many dissolved salts, predominantly sodium chloride; silicon is deliberately doped with other chemicals during the production of semi-conducting crystals; and copper is mixed with lead or zinc to produce bronze or brass. In common parlance, the word alloy is usually only ascribed to metallic mixtures. But, in terms of the way these liquids solidify, at least as far as the macroscopic issues of heat and solute transport are concerned, all multi-component liquids can be considered as alloys. Though many melts of interest (molten lavas and modern 'super alloys', for example) are composed of several distinct species, much of the fundamental behaviour of solidifying alloys can be learned from a study of alloys composed of just two species, so-called binary alloys, and that will be our focus here.

We shall further confine our attention to simple *binary eutectics*. These are characterized by having a phase diagram similar to that depicted in figure 5 and include many systems of interest: most aqueous salt solutions; many metallic alloys; and a number of mineral mixtures. Their predominant characteristic is that they remain liquid at temperatures lower than the freezing temperature of either of their pure constituents. A well-known example of this is that salt water remains liquid at sub-zero temperatures, which is why
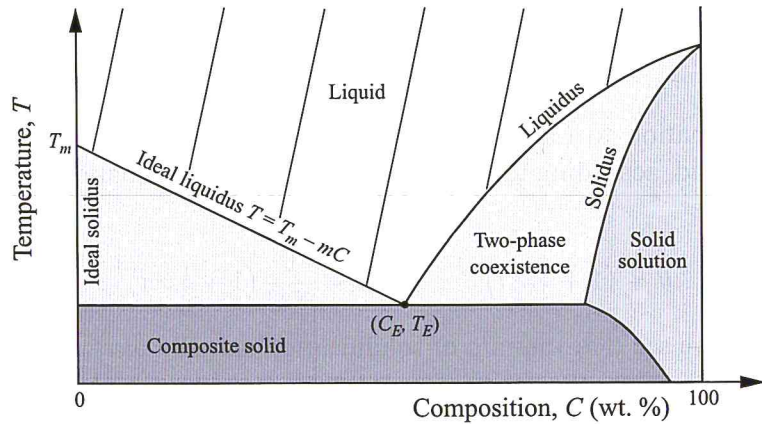
Figure 5. The equilibrium phase diagram of a typical eutectic binary alloy. The shaded regions show what phases exist in equilibrium in a sample of bulk composition C and uniform temperature T. When the temperature is above the liquidus curve, the sample is completely liquid. The almost vertical lines in this region of the diagram are density contours. The density of the liquid decreases as the temperature increases but increases more strongly as the concentration of the liquid increases. In the region between the liquidus and the solidus, solid and liquid can co-exist in equilibrium, with the composition of the liquid phase equal to the liquidus concentration and the composition of the solid phase equal to the solidus concentration at the given temperature. This is the state of the interior of an ideal mushy layer (§ 6). In general the solid phase is a *solid solution* of the two components of the alloy: molecules of one component of the alloy are incorporated within the lattice of the other. In many cases the lattice parameters are such that solid solutions are not possible and the solid phase is almost pure, as shown on the left of the diagram. Below the eutectic temperature T_E a composite solid forms composed of crystals of both of the end members of the alloy. In many mathematical studies the liquidus is taken to be linear, as shown on the left.

salt is scattered onto icy roads. The temperature at which an alloy begins to freeze is called the liquidus temperature $T_L(C)$, which is a function of the composition C of the melt. [Throughout the remainder of this chapter we shall denote by C the concentration (in weight percentage) of that component which makes the melt more dense. In the case of salt water, for example, C will denote the concentration of salt.] Another common experience is that adding water to salt causes the salt to dissolve – again, the mixture is liquid at a temperature well below the melting temperature of pure salt (801°C). The two liquidus curves, that defining the freezing-point depression of water by the addition of salt and that defining the freezing-point depression of salt by the addition of water, meet at the *eutectic point*, which determines the lowest temperature T_E at which the alloy can be fully molten, and occurs at

a specific concentration C_E. The eutectic point of salt water, for example has a temperature of $-21.1°C$ and is achieved at a concentration of 23.3 wt. % NaCl.

Another characteristic feature of the way that alloys solidify, and the one that leads to the most interesting fluid-mechanical effects, is that the solid formed has a composition different from that of the melt: ice growing from salt water is almost pure, for example. As a result of this, the component that is rejected by the solid builds up ahead of the solidification front and must be transported away in order for solidification to proceed. We shall see that the build-up of solute not only inhibits growth but promotes morphological instability and can drive compositional convection in the melt.

The solid that forms at temperature T has a composition given by the solidus relationship $C = C_S(T)$, shown in figure 5. It is often expressed as $C_S(T) = k_D C_L(T)$, where C_L is the liquidus concentration and k_D is called the distribution (or segregation) coefficient.

4.1 An extended Stefan problem

The simple one-dimensional models analysed in §2 can be extended to the case of a solidifying binary alloy. For simplicity, consider the case that the distribution coefficient is zero so that the solid formed is pure, with concentration $C_S = 0$. The concentration $C(z,t)$ of the melt is governed by the diffusion equation

$$\frac{\partial C}{\partial t} = D \frac{\partial^2 C}{\partial z^2} \tag{4.1}$$

and satisfies boundary conditions

$$C \to C_0 \quad (z \to \infty), \tag{4.2}$$

$$C = C_i, \quad (C - C_S)\dot{h} = -D \frac{\partial C}{\partial z}\Big|_{z=h+} \quad (z = h(t)), \tag{4.3a, b}$$

where C_i is the unknown concentration of the melt at the solidification front. Equation (4.3b) expresses conservation of solute at the front: the left-hand side gives the rate at which solute is rejected by the advancing solid, while the right-hand side gives the diffusive flux of solute from the front into the melt. The temperature field satisfies the diffusion equation (2.3) in both solid and liquid, and boundary conditions

$$T = T_B \quad (z = 0), \quad T \to T_\infty \quad (z \to \infty), \tag{4.4}$$

$$T = T_i, \quad \rho L \dot{h} = k \frac{\partial T}{\partial z}\Big|_{z=h-} - k \frac{\partial T}{\partial z}\Big|_{z=h+} \quad (z = h(t)). \tag{4.5a, b}$$

To close the system, the interfacial temperature and melt concentration are related by

$$T_i = T_L(C_i) \equiv T_m - mC_i,\tag{4.6}$$

where, for simplicity, we have assumed that the liquidus curve is linear with constant slope $-m$, as shown on the left in figure 5.

These equations and boundary conditions admit a similarity solution

$$h = 2\lambda\sqrt{Dt},\tag{4.7}$$

$$T = T_B + (T_i - T_B)\frac{\mathrm{erf}\,\epsilon\eta}{\mathrm{erf}\,\epsilon\lambda}\qquad (\eta < \lambda),\tag{4.8}$$

$$T = T_\infty + (T_i - T_\infty)\frac{\mathrm{erfc}\,\epsilon\eta}{\mathrm{erfc}\,\epsilon\lambda}\qquad (\eta > \lambda),\tag{4.9}$$

$$C = C_0 + (C_i - C_0)\frac{\mathrm{erfc}\,\eta}{\mathrm{erfc}\,\lambda}\qquad (\eta > \lambda)\tag{4.10}$$

in terms of the similarity variable

$$\eta = \frac{z}{2\sqrt{Dt}}.\tag{4.11}$$

The coefficient λ is determined from the coupled equations

$$C_i = \frac{C_i - C_0}{F(\lambda)}, \qquad \frac{L}{C_p} = \frac{T_i - T_B}{G(\epsilon\lambda)} - \frac{T_\infty - T_i}{F(\epsilon\lambda)},\tag{4.12a,b}$$

derived from (4.3b) and (4.5b) respectively, by eliminating C_i and T_i using (4.6), where the functions G and F are as defined in (2.8) and (2.14). Note that the thickness of the solid $h(t)$ has been scaled with the length scale for solutal diffusion $\sqrt{Dt}$. This length scale is much smaller than that for thermal diffusion, $\sqrt{\kappa t}$, since the Lewis number, $Le \equiv \kappa/D \equiv \epsilon^{-2}$, is typically very large (e.g. $Le \simeq 80$ for salt water). In the limit $\epsilon \ll 1, F(\epsilon) \sim \sqrt{\pi}\epsilon$ and $G(\epsilon) \sim 2\epsilon^2$. Equation (4.12b) then gives

$$T_i \simeq T_B + O(\epsilon),\tag{4.13}$$

whence

$$F(\lambda) \equiv \sqrt{\pi}\lambda e^{\lambda^2}\mathrm{erfc}\,\lambda \simeq \mathscr{C}^{-1}, \qquad \text{where} \qquad \mathscr{C} = \frac{C_S - C_B}{C_0 - C_B},\tag{4.14}$$

and $C_B = C_L(T_B)$.

This expression is similar to (2.14), obtained for growth of solid from an undercooled pure melt, but with $\mathscr{C}$ replacing the Stefan number S. Note that $\mathscr{C}$ is always greater than unity (except when the melt is pure) so that
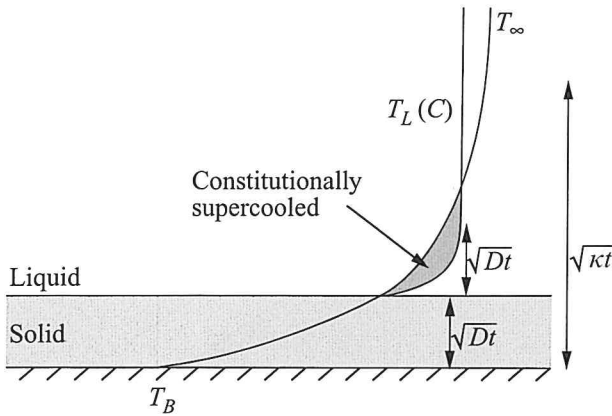
Figure 6. A schematic diagram of the one-dimensional solidification of a binary alloy. The rate of solidification is limited by the rate of transport of solute away from the interface where it is rejected. The solute accumulates in a compositional boundary layer causing a local depression of the freezing temperature. Since heat diffuses much more rapidly than solute ($\kappa \gg D$), a region of constitutional supercooling results, as shown.

finite solutions to (4.14) always exist. This confirms that $a(t)$ does indeed scale with $\sqrt{Dt}$ when D/κ is small; the rate of solidification of an alloy is controlled by the rate of transport of solute.

The concentration ratio $\mathscr{C}$ is a very important parameter in alloy solidification. It is best described in words as the ratio of the typical difference in concentration between the solid and the liquid to the scale for concentration variations with the liquid, though it may have slightly different mathematical expressions in different circumstances. It is analogous for concentration to the Stefan number for heat (enthalpy). Recall that the Stefan number is the ratio of the difference in enthalpy (latent heat) between the solid and the liquid to the scale for enthalpy variations (sensible heat) within the liquid. The analogy manifests itself mathematically in the similarity between equations (2.14) and (4.14), for example. We shall see later that $\mathscr{C}$ also plays a dominant role in determining the fraction of solid present in a partially solidified alloy.

4.2 Constitutional supercooling

The similarity between the solidification of an alloy and the solidification of a supercooled pure melt does not end with the comparability between (4.14) and (2.14). The accumulation of rejected solute ahead of the solidification front lowers the local freezing temperature there, as shown in figure 6.
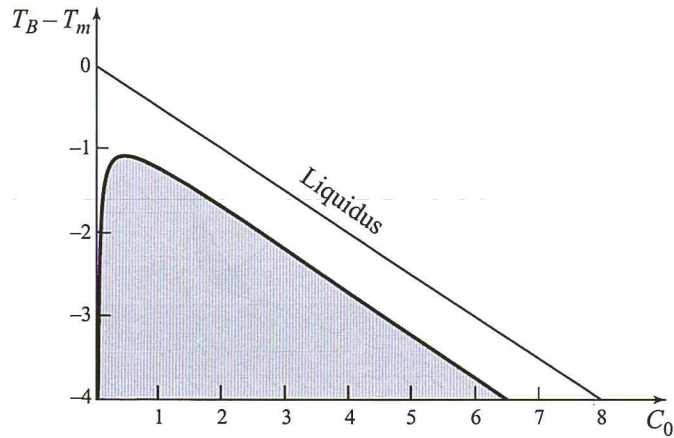
Figure 7. The shaded region shows the conditions (initial concentration C_0 and boundary temperature T_B) under which constitutional supercooling will occur in the melt during one-dimensional solidification from a cooled boundary. Very small amounts of solute lead to constitutional supercooling even when the boundary temperature is not much below the liquidus and the solidification is rather slow. The curve shown was calculated with $T_\infty = 20°C, m = 0.5°C \text{ wt.}\%^{-1}, \epsilon = 0.05$ and $L/C_p = 80°C$, which are typical values for ice growing from an aqueous salt solution.

Since the thermal boundary layer is much broader than the compositional boundary layer, the temperature within the compositional boundary layer remains close to the interfacial temperature. As a result of this, the temperature is lower than the local freezing temperature throughout most of the compositional boundary layer; the liquid is said to be locally, *constitutionally* supercooled.

Constitutional supercooling is a driving force for morphological instability. In this case, the thermal field and the surface energy are both stabilizing, so the criterion for morphological instability (Mullins & Sekerka 1964) is not coincident with that for constitutional supercooling, though they are close. In the present case, constitutional supercooling occurs when $G \equiv (\partial T/\partial z)_{z=h+} < -m(\partial C/\partial z)_{z=h+} \equiv -mG_c$, i.e. when

$$\frac{\epsilon^2(T_\infty - T_i)}{F(\epsilon\lambda)} < \frac{m(C_i - C_0)}{F(\lambda)} . \tag{4.15}$$

A graph of this inequality, figure 7, shows that constitutional supercooling is a very common occurrence in naturally solidifying systems. The result is often the formation of a mushy region, which will be described in §6. By carefully controlling the conditions of the melt and the rate of solidification, it is possible to inhibit constitutional supercooling and morphological

instability. This is a major concern of those producing single crystals for the semi-conductor industry and forms the topic of the next section.

5 Morphological instability and flow

Industrial crystal growers producing large single semi-conductor crystals are severely constrained by the need to suppress morphological instability. We have seen that it is the accumulation of rejected solute ahead of the solidification front that causes constitutional supercooling and hence promotes instability. This has given some hope that fluid flow, by enhancing solute transport, can be used to control instability and allow faster production rates of purer crystals. Some of the fundamental principles are presented here. Much fuller accounts can be found in reviews by Glicksman, Coriell & McFadden (1986) and Davis (1990).

5.1 Morphological instability

Thus far, we have considered situations in which a solid has been growing from a fixed cooled boundary. In this section we shall concentrate on a crystal-growing configuration in which a melt is pulled slowly at a constant speed V through a prescribed linear temperature field with gradient G. Since crystal growth rates are controlled by solute transport, and we shall therefore be focusing on the compositional boundary layer, it is convenient to work with the 'frozen-temperature' approximation that the temperature field is constant and given by $T(z,t) = T_i + Gz$ in a frame of reference fixed with respect to the coolers.

Diffusion of solute in the solid phase is typically very slow, so the concentration field is 'frozen in' at the solid–liquid interface ($z = \zeta(x,t)$). The concentration of the melt, however, is governed by the advection–diffusion equation

$$\frac{\partial C}{\partial t} - V\frac{\partial C}{\partial z} = D\nabla^2 C. \tag{5.1}$$

It is further constrained by the interfacial solute-conservation equation (4.3b), which becomes

$$C(1 - k_D)(V + \zeta_t) = -D\mathbf{n} \cdot \nabla C \quad (z = \zeta), \tag{5.2}$$

and the Gibbs–Thomson relationship (2.19), modified by the liquidus relationship to become

$$T = T_m - mC - \Gamma\nabla \cdot \mathbf{n} \quad (z = \zeta). \tag{5.3}$$

These equations, together with the far-field condition, $C \to C_0$ as $z \to \infty$, have a steady one-dimensional solution with $\zeta = 0$ and

$$C = C_0 + C_0 \left(\frac{1 - k_D}{k_D} \right) e^{-Vz/D} . \tag{5.4}$$

Morphological stability of this system can be examined by considering the perturbed solutions

$$C = C_0 + C_0 \left(\frac{1 - k_D}{k_D} \right) e^{-Vz/D} + \hat{\phi} e^{-\mu Vz/D} e^{i\alpha x' + \sigma t'}, \qquad \zeta = \hat{\zeta} e^{i\alpha x' + \sigma t'} \tag{5.5}$$

where $x' = Vx/D$, $t' = V^2 t/D$, α and σ are all dimensionless and the constant μ is determined from (5.1) to be

$$\mu = \tfrac{1}{2} \left[1 + \sqrt{1 + 4(\alpha^2 + \sigma)} \right] . \tag{5.6}$$

Equations (5.2) and (5.3) are linearized to give

$$-G_c \sigma \hat{\zeta} = k_D G_c \hat{\zeta} + (\mu - 1 + k_D) \hat{\phi} \tag{5.7}$$

and

$$G \hat{\zeta} = -m G_c \hat{\zeta} - m \hat{\phi} - \alpha^2 \frac{\Gamma V^2}{D^2} \hat{\zeta} , \tag{5.8}$$

where

$$G_c = -C_0 \frac{1 - k_D}{k_D} \frac{V}{D} < 0 \tag{5.9}$$

is the concentration gradient in the melt at the undisturbed solid–liquid interface. These equations combine to give the growth rate implicitly (since $\mu = \mu(\sigma)$) by

$$\sigma = -k_D + (\mu - 1 + k_D) \left(1 - M^{-1} - \frac{l_\Gamma}{l_C} \alpha^2 \right) , \tag{5.10}$$

where $M = -mG_c/G$ is the morphological number, $l_C = D/V$ is the solutal diffusion length and

$$l_\Gamma = \frac{\Gamma k_D}{mC_0 (1 - k_D)} \tag{5.11}$$

is a capillary length. Equation (5.10) gives a rather complicated relationship for the growth rate σ. However, it can be shown that its key features occur when $\alpha \gg 1$, with $\sigma = O(\alpha)$, whence $\mu \sim \alpha$ (from (5.6)) and

$$\sigma \sim -k_D + \alpha \left(1 - M^{-1} - \frac{l_\Gamma}{l_C} \alpha^2 \right) . \tag{5.12}$$

Note that the first term on the right-hand side is retained even though $\alpha \gg 1$,

since the term in brackets can be small near marginal stability. From this simpler expression it is readily determined that morphological instability occurs ($\sigma > 0$) when

$$M^{-1} < 1 - \frac{l_\Gamma}{l_C}\alpha^2 - \frac{k_D}{\alpha} \ . \tag{5.13}$$

The minimum value of M for which morphological instability can occur is therefore M_c, where

$$M_c^{-1} = 1 - \frac{3}{2}\left(2k_D^2\frac{l_\Gamma}{l_C}\right)^{1/3} , \tag{5.14}$$

i.e. instability occurs when M is slightly larger than unity and the melt is constitutionally supercooled.[1]

Equation (5.12) shows further that as M is increased above M_c the first modes to become unstable have wavenumber

$$\alpha = \left(\frac{k_D}{2}\frac{l_C}{l_\Gamma}\right)^{1/3} , \tag{5.15}$$

which corresponds to a (dimensional) wavelength

$$\lambda_c = 2\pi\left(\frac{2}{k_D}\right)^{1/3}\left(l_C^2 l_\Gamma\right)^{1/3} \ . \tag{5.16}$$

In contrast, once the stability threshold has been significantly exceeded the modes with maximum growth rate ($\partial\sigma/\partial\alpha = 0$) have a much shorter wavelength

$$\lambda_{\max} = 2\pi\left(\frac{3M}{M-1}\right)^{1/2}(l_C l_\Gamma)^{1/2} \ . \tag{5.17}$$

This expresses a result similar to (2.25), namely that the wavelength of maximum growth is proportional to the geometric mean of a diffusion length (here the solutal diffusion length) and a capillary length. The disparity in length scale between the marginally stable modes and the modes of maximum growth rate can be reconciled using (5.17) by recalling that M is only slightly larger than unity near marginal stability, as expressed by (5.14).

One of the most important results of this analysis is that instability is enhanced by increasing the solutal gradient, i.e. by thinning the compositional boundary layer. We shall examine the effects of various flows on the compositional boundary layer and hence deduce their influence on morphological instability. Another important result is that the characteristic length

---

[1] This situation can be reversed – the interface can be morphologically unstable while the melt is not constitutionally supercooled – in certain circumstances when the thermal conductivity of the solid is greater than that of the liquid.

M. G. *Worster*

(a)

(b)

(c)   Basic flow   (d)   Secondary flow

        Wave propagation   Wave propagation
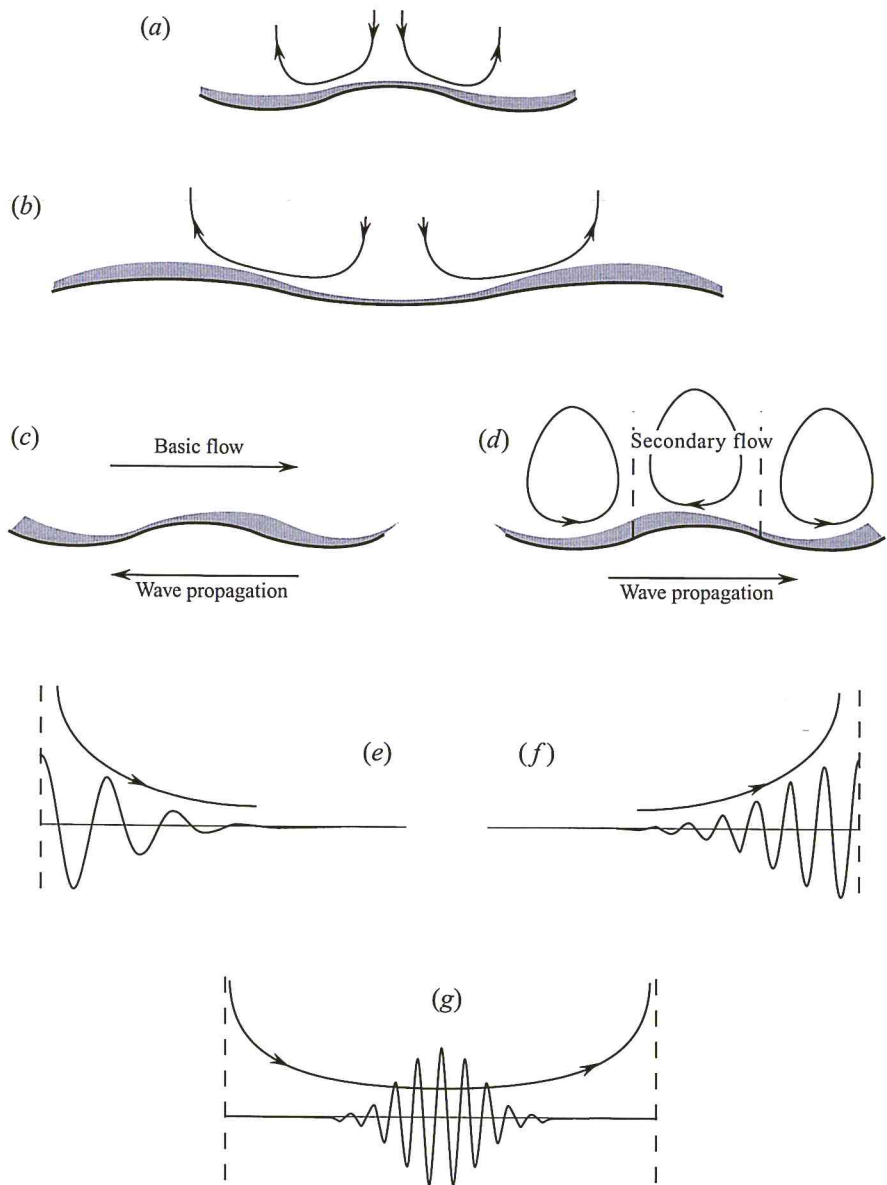
(e)   (f)

(g)

Figure 8. For caption see facing page.

scale (wavelength) of morphological instabilities is much smaller than the thickness of the compositional boundary layer (since typically $l_\Gamma \ll l_C$), which often limits the ability of flow to control morphological instability, as will be described below.

5.2 Natural compositional convection

The variation in concentration within the compositional boundary layer causes density gradients that, in a gravitational field, can drive natural buoyant convection. Consider first the case that solidification is upwards and the rejected solute is dense, for example by freezing ice from a salt solution by cooling it from below. The compositional boundary layer is statically stable to buoyancy-driven convection. However, if the solid–liquid interface becomes corrugated then the dense fluid flows down into the valleys, as shown in figure 8(a). A stagnation point with flow towards the solid is formed at the top of each crest, which, as we saw in § 3.1, thins the boundary layer and promotes solidification there; morphological instability is enhanced.

If the rejected solute is buoyant then the compositional boundary layer is statically unstable but may be dynamically stable if its Rayleigh number is less than critical (see Chapter 6). In this case, the flow depicted in figure 8(a) is reversed and morphological instability is delayed.

Once the Rayleigh number associated with the compositional boundary layer exceeds its critical value, convection occurs regardless of any deformation of the interface. The solute-conservation equation (5.2) shows that in a steadily convecting state the concentration of the melt at the interface is greatest where the solute gradient is steepest, i.e. where the boundary layer is thinnest. Consequently the equilibrium temperature is lowest at such places and the interface is depressed as shown in figure 8(b). This is not a morphological instability as such, because morphological changes are not

---

Figure 8. The effects of flow on morphological instabilities. In all cases solidification is upwards. (a) If the rejected solute is dense its buoyancy drives a flow from crests to troughs, which thins the boundary layer above crests and promotes morphological instability. (b) Steady compositional convection resulting from rejection of a buoyant solute on scales larger than typical morphological modes depresses the interface in regions of downflow. Morphological instabilities on smaller length scales are enhanced slightly within such depressions. (c) A steady shear flow compresses the compositional boundary layer on the upstream faces of interfacial corrugations causing them to propagate upstream. (d) The secondary flow arising from the need to satisfy the no-slip condition at the perturbed interface compresses the boundary layer on the downstream faces and causes the perturbations to propagate downstream. The first of these effects dominates at long wavelengths, the second at short wavelengths. Thus given a pure stagnation-point flow, long waves are found near diverging stagnation points (e) while short waves are found near converging stagnation points (f). In a completely confined flow, an absolute instability is found between stagnation points at stationary points of the horizontal components of the imposed flow (g).

intrinsic to the instability, but is rather a response of the interface to the convective flow. Whereas a morphological instability will develop into cellular and ultimately dendritic structures, the interface deformation resulting from convective motions may become less pronounced as further convective instabilities occur and turbulent motions ensue.

It is important to note that the length scale of convective instabilities is comparable to the thickness of the solutal boundary layer l_C and is therefore much longer than the scale of morphological instabilities $(l_C^2 l_\Gamma)^{1/3}$. Consequently any coupling between the two is weak, and it has been found that natural convection cannot be exploited effectively to control morphological instabilities during crystal growth. Researchers have therefore turned their attention to various forced flows in an effort to find a way of controlling instability.

5.3 Forced flows

Since the Schmidt number $Sc = v/D$ of most materials is very large, the compositional boundary layer at a solidification front is normally subsumed within the viscous boundary layer and the flow is locally linear. Therefore, away from confining boundaries and stagnation points, all flows can be approximated by a simple parallel shear flow on the scale of morphological instabilities.

The primary influence of a simple shear is shown in figure 8(c, d). The horizontal basic flow compresses the perturbed solutal boundary layer on the upstream faces of a perturbed interface, as shown in figure 8(c), which promotes the normal growth of those faces and results in a wave-like propagation of the perturbation upstream. Countering this tendency is the secondary flow induced by the need to satisfy the no-slip condition on the perturbed interface. The secondary flow has stagnation points between crests and troughs that compress the basic solutal boundary layer on downstream faces and thus promote a downstream propagation of the interface perturbation (figure 8d). The first of these effects dominates at long wavelengths $\lambda > \lambda_a$ (say), while the second dominates at the shorter wavelengths ($\lambda < \lambda_a$) characteristic of morphological instabilities. Forth & Wheeler (1989) have calculated the dispersion relation for these travelling waves and have shown that λ_a is typically of the same order of magnitude as the thickness of the compositional boundary layer l_C. In both cases the enhancement of solidification is $\pi/2$ out of phase (either negative or positive) with the interface perturbation and therefore has a neutral influence on instability. This is the dominant behaviour for large Schmidt number. At higher orders in inverse

Schmidt number, more complex interactions result in a weak suppression of the two-dimensional morphological instability. The flow has no effect on the conditions for instability of perturbations with crests aligned parallel to the direction of flow, however, so these are the preferred modes near marginal conditions.

These results on an infinite domain indicate that morphological instability in the presence of flow is *convective* (see Chapter 4) and care is needed to apply them to an understanding of what will happen in a finite domain.

In confined systems, there are stagnation points at which the tangential flow is zero. Brattkus & Davis (1988) carried out an analysis restricted to long-wavelength disturbances and found instabilities at *diverging* stagnation points, which is consistent with the fact that long waves travel upstream towards the stagnation point (figure 8e). Conversely, Bühler & Davis (1998), found that disturbances of wavelengths comparable to those of morphological instability in the absence of flow (i.e. much smaller than λ_a) are localized near *converging* stagnation points, again consistent with the fact that such waves travel downstream, towards the stagnation point (figure 8f)[1]. However, in a system confined at both ends the most *absolutely* unstable mode occurs at wavelengths such that $\partial \omega / \partial k = 0$ and at positions where $\partial \omega / \partial x = 0$ (see Chapter 4). Given the dispersion relation derived by Forth & Wheeler (1989) in which ω is directly proportional to the free-stream flow U, the latter occurs where $\partial U / \partial x = 0$, i.e. between stagnation points (figure 8g).

Overall, it seems that steady flows may do little to suppress morphological instability and can even enhance it in certain circumstances, but it can alter the characteristics of the unstable modes and may serve to confine instabilities to a small region of a growing crystal. Certain types of unsteady flows, for example orbital flows (Schulze & Davis 1995), seem more promising in controlling morphological instability.

6 Mushy layers

In most natural and metallurgical settings, solidification rates greatly exceed the critical values required for morphological instability. Planar interfaces cannot survive the build-up of solute and consequent constitutional super-cooling ahead of them, and give way to highly convoluted solid structures that form the matrix of a porous medium called a mushy layer (figure 9). The solute rejected during solidification no longer needs to be transported

[1] Strictly figure 8(e, f) and the associated discussion relate to the phase velocity of the perturbations. The analysis of Forth & Wheeler shows also that the group velocity of long waves is upstream and for short waves is downstream.
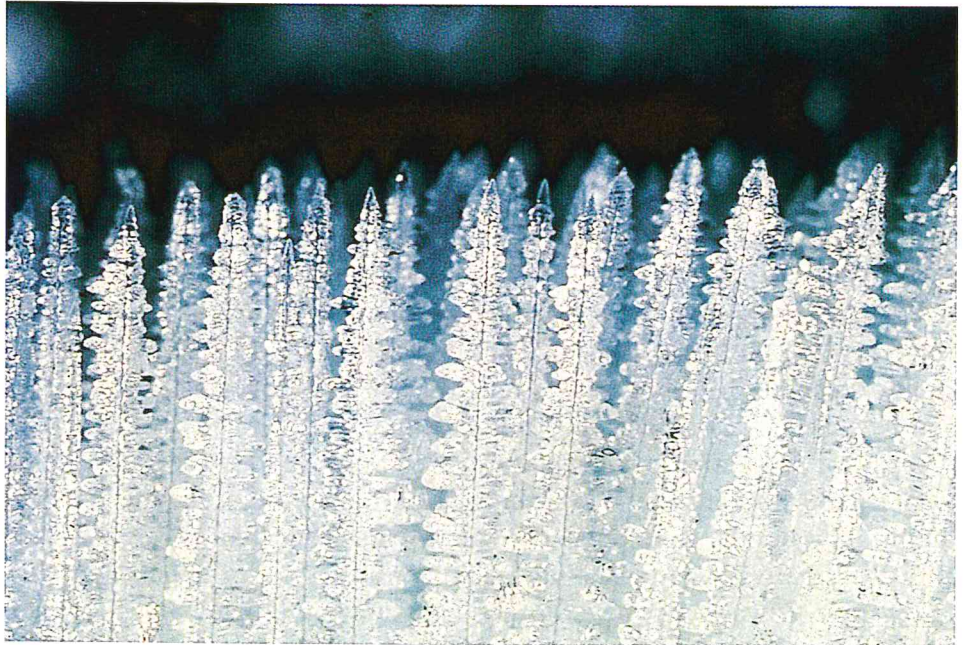
Figure 9. A close-up view of the interfacial region of a dendritic mushy layer. The solid phase in this case is ammonium chloride. The spacing between dendrites is about 0.3 mm while the overall depth of the mushy layer is a few centimetres.

into the bulk liquid region but can be accommodated within the interstices (pores) of the mushy layer. Local solute transport continues to play a role on the scale of individual pores, determining the size of the pores and the occurrence of side branches on the crystals forming the matrix, but the macroscopic evolution of a mushy layer is controlled predominantly by thermal balances. The structure of a mushy layer is affected by fluid motions in the melt adjacent to it and in the melt flowing through its interstices.

6.1 Relief of supercooling

We saw in §4 that a region of constitutional supercooling can develop in an alloy ahead of a solidification front. The effect of morphological instabilities is to increase the surface area of the phase boundary and thus to enhance both the liberation of latent heat and the rejection of solute. The former tends to warm the melt while the latter causes a lowering of the local freezing temperature (liquidus). These each serve to reduce the degree of constitutional supercooling. Without surface energy, morphological instabilities would occur on arbitrarily small length scales given any amount

of supercooling, and it is not hard to imagine therefore that this process would continue until the degree of constitutional supercooling were reduced to zero. In practice, surface energy limits instability at some scale, as we have seen. But if the surface energy is small ($l_\Gamma \ll l_C$) then it is a good approximation to assume that the temperature and concentration of the interstitial liquid in a mushy layer lie on the liquidus

$$T = T_L(C). \tag{6.1}$$

There is some experimental support for this assumption and to date it has been almost universally adopted in mathematical models of mushy layers.

6.2 Evolution of a mushy layer without flow

The primary feature of a mushy layer is the accommodation of excess solute within its interstices and the loss thereby of solutal control on its overall extent. We can gain an understanding of this by considering a simple model in which we imagine that the mushy layer has a uniform volume fraction of solid ϕ. When the solid is pure ($C_S = 0$) and there is no fluid flow, the total amount of solute within the layer per unit horizontal area is

$$\int_0^{h(t)} (1-\phi)C_L(T)\mathrm{d}z = hC_0 \, , \tag{6.2}$$

where $h(t)$ is the depth of the layer and $T(z,t)$ is the local temperature. If we make the quasi-stationary approximation then

$$T \simeq T_B + (T_L(C_0) - T_B)\frac{z}{h(t)} \tag{6.3}$$

and equation (6.2) then shows that

$$\phi = \frac{C_L(T_B) - C_0}{C_L(T_B) + C_0} \equiv \frac{1}{2\mathscr{C} - 1}, \tag{6.4}$$

assuming that the liquidus is linear, where $\mathscr{C}$ is the important concentration ratio introduced in equation (4.14).

Note that $\phi = 1$ when $C_0 = 0$ ($\mathscr{C} = 1$), corresponding to a pure melt, and that ϕ is small for large values of $\mathscr{C}$, a fact exploited in many analyses of mushy layers.

The Stefan condition at the mush–liquid interface is

$$\phi\rho_s L\dot{h} = \bar{k}(\phi)\frac{\partial T}{\partial z}\bigg|_{z=h-} = \bar{k}(\phi)\frac{T_L(C_0) - T_B}{h}, \tag{6.5}$$
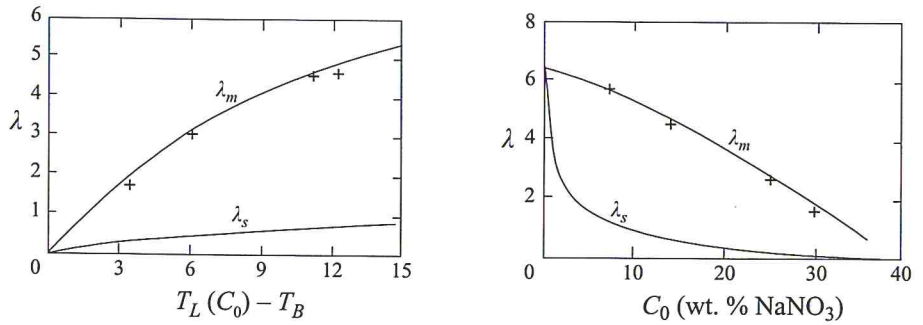
Figure 10. The rates of diffusion-controlled solidification of a binary alloy from a cooled boundary. A planar solid–liquid interface is predicted to advance as $h = 2\lambda_s\sqrt{Dt}$, where λ_s is determined from (4.14), while a mush–liquid interface is predicted to advance as $h = 2\lambda_m\sqrt{Dt}$, where λ_m is determined by an extension of the theory leading to (6.7). This theory (Huppert & Worster 1985) gives very good agreement with the data (crosses) from experiments in which mushy layers of ice crystals were formed by cooling aqueous solutions of sodium nitrate from below.

where

$$\bar{k}(\phi) = \phi k_s + (1 - \phi)k_l \tag{6.6}$$

is a mean thermal conductivity of the mushy layer, and the heat flux from the melt has been ignored. This mean conductivity is exact for a medium composed of lamellae oriented parallel to the heat flux vector (Batchelor 1974) and is a good approximation within mushy layers since the crystals forming the solid matrix have primary branches aligned with the local heat flux vector. Equation (6.5) is readily integrated to yield

$$h = \left(\frac{2}{S}\frac{\bar{k}}{k_s\phi}\kappa_s t\right)^{1/2}, \tag{6.7}$$

where the Stefan number $S = L/C_{ps}[T_L(C_0) - T_B]$, $\kappa_s = k_s/\rho_s C_{ps}$ and C_{ps} is the specific heat capacity of the solid. This result, which can be compared with (2.11) and contrasted with (4.7), highlights the fact that the growth of the mushy layer is determined by the rate of *thermal* diffusion. To make accurate predictions, care is needed in estimating the appropriate thermal conductivity of the layer. Note, for example, that the thermal conductivity of ice is about four times that of water so the mean conductivity of the mushy layer is sensitive to the solid fraction.

A slightly more detailed model along the lines above (Huppert & Worster 1985) has given results in good agreement with laboratory experiments (figure 10).

6.3 Flow in a mushy layer

The interstitial liquid within a mushy layer is free to flow in response to pressure gradients and buoyancy forces. The characteristics of its flow are fundamentally those of flows within porous media (Phillips 1991; Nield & Bejan 1999), the simplest model of which is given by Darcy's equation

$$\mu\boldsymbol{u} = \boldsymbol{\Pi}(-\nabla p + \rho\boldsymbol{g}).\tag{6.8}$$

Here $\boldsymbol{u}$ is the 'superficial' velocity or 'Darcy' velocity, which is the volume flux per unit area flowing through the medium, p is the pressure and $\boldsymbol{g}$ is the acceleration due to gravity. The permeability $\boldsymbol{\Pi} = \boldsymbol{\Pi}(\phi, \mathscr{A})$ is a second-rank tensor, reflecting the fact that the resistance to flow within the medium may be anisotropic, and is a function both of the void fraction $1 - \phi$ and the specific surface area $\mathscr{A}$ of the internal phase boundaries as well as their geometry. In many studies the permeability is assumed to be locally isotropic and the dependence on $\mathscr{A}$ is ignored for no better reason than it is a difficult quantity both to measure and to predict. We shall assume here that $\boldsymbol{\Pi} = \Pi(\phi)\boldsymbol{I}$, where $\boldsymbol{I}$ is the identity.

What distinguishes the flow in a mushy layer from that in a passive porous medium is that the solid fraction and hence its porosity can vary both in time and in space. This has two significant consequences. The first is that, as indicated above, the permeability is spatially inhomogeneous and may vary in time. We shall see later that this can lead to an interesting feedback between flow and solidification in mushy layers, typically resulting in a focusing of flows into narrow regions of low (or even zero) solid fraction. The second is that the velocity field in a mushy layer is non-solendoidal. Local mass conservation is expressed by

$$\frac{\partial\overline{\rho}}{\partial t} + \nabla \cdot (\rho_l \boldsymbol{u}) = 0,\tag{6.9}$$

where the mean density $\overline{\rho} = \phi\rho_s + (1 - \phi)\rho_l$, which can be rearranged as

$$\nabla \cdot \boldsymbol{u} = -\frac{\rho_s - \rho_l}{\rho_l}\frac{\partial\phi}{\partial t}.\tag{6.10}$$

This shows that there is a divergence of the flow as solid grows internally if $\rho_s < \rho_l$ so that there is an expansion on change of phase, as is the case for water and for silicon, for example. Conversely, many other materials contract as they solidify, which leads to a convergent flow. Clearly fluid flow is driven by this mechanism even in the absence of external forces. It can cause redistribution of solute within a casting and, in the case of contraction, can cause voids to form (see Beckermann & Wang 1995, for

example). Though these are interesting effects we shall not explore them further and set $\rho_s = \rho_l$ so that $\nabla \cdot \boldsymbol{u} = 0$.

6.4 Response to an external flow

An interesting example of how the interstitial liquid can be driven by external pressure gradients is provided by a study of the morphological stability of the mush–liquid interface (the envelope of the solid matrix) in the presence of an external flow. To focus attention on the interfacial region, consider a semi-infinite mushy layer of uniform solid fraction ϕ in $z < 0$, adjacent to a liquid region ($z > 0$) flowing with uniform velocity U parallel to the interface. Consider the response to a small perturbation to the interface, $z = \zeta = \hat{\zeta} e^{i\alpha x + \sigma t}$ and, for simplicity, imagine that the flow in the liquid region is an irrotational flow $\boldsymbol{u} = \nabla \Phi$ with $\nabla^2 \Phi = 0$. The flow in the mushy region is much slower than that in the liquid, so to a leading approximation we can treat the mushy layer as impermeable to the external flow ($\boldsymbol{n} \cdot \nabla \Phi = 0$ on $z = \zeta$) and calculate that

$$\Phi = Ux - iU\zeta e^{-\alpha z}. \tag{6.11}$$

The linearized Bernoulli's equation then gives the pressure at the interface to be

$$p = -\rho \alpha U^2 \zeta. \tag{6.12}$$

There is low pressure above the crests and higher pressure above the troughs, and it is this pressure difference that drives a flow in the mushy layer (figure 11). In the absence of gravity and with ϕ constant, equation (6.8) combined with the equation of continuity, $\nabla \cdot \boldsymbol{u} = 0$, shows that the pressure in the mushy layer is harmonic, $\nabla^2 p = 0$, and equal to

$$p = -\rho \alpha U^2 \zeta e^{\alpha z}. \tag{6.13}$$

If we take the temperature field to be $T = Gz + \hat{\theta}(z) e^{i\alpha x + \sigma t}$, a perturbation from a linear gradient, the quasi-stationary thermal advection–diffusion equation gives

$$\kappa (D^2 - \alpha^2)\hat{\theta} = G\frac{\Pi}{\nu}\alpha^2 U^2 \hat{\zeta} e^{\alpha z}, \tag{6.14}$$

where, here, $\kappa = \bar{k}/\rho_l C_{pl}$ and C_{pl} is the specific heat of the liquid. This has solution

$$\hat{\theta} = \frac{G\Pi\alpha U^2}{2\kappa\nu}\hat{\zeta} z e^{\alpha z} - G\hat{\zeta} e^{\alpha z}, \tag{6.15}$$

since T is fixed at the interface by the liquidus constraint. Finally, the Stefan
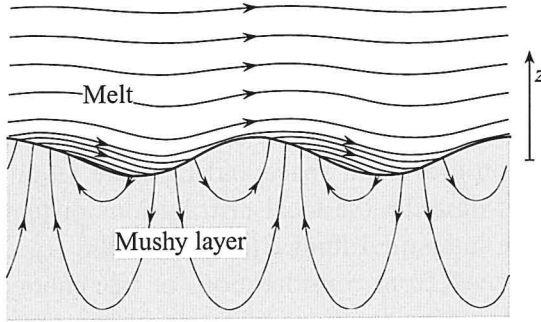
Figure 11. A schematic diagram showing the influence of an external flow on the evolution of a mushy layer. The streamlines in the melt are compressed over crests. The resulting low pressure there drives a flow in the mushy layer that interacts with the thermal field to drive a morphological instability of the interface. Note that in the liquid region away from the neighbourhood of the interface only every fourth streamline has been plotted for clarity.

condition (6.5) gives

$$\sigma = \frac{\bar{k}(\phi)}{\rho L \phi} \alpha G \left[-1 + \frac{\Pi U^2}{2 \kappa v} \right]. \tag{6.16}$$

This simple analysis shows that there is instability at all wavelengths if the dimensionless group

$$\frac{\Pi U^2}{\kappa v} > 2 , \tag{6.17}$$

i.e. if the external flow is sufficiently rapid. A more detailed analysis (Feltham & Worster 1999) shows that long wavelengths are stable given a mushy layer of finite depth, that the short wavelengths are stable when the external flow is a viscous shear rather than an inviscid uniform flow and that the most unstable wavelengths are comparable to the depth of the layer.

More generally, dimensional analysis shows that a high-Reynolds-number external flow has a significant influence on the evolution of the mushy layer if

$$\mathcal{U}^2 \gtrsim \sigma Da^{-1}, \tag{6.18}$$

where $\mathcal{U} = U/V$, V is the solidification rate and the Darcy number $Da = \Pi/L^2$ is the ratio of the permeability to the square of the macroscopic lengthscale $L = \kappa/V$, which is consistent with (6.17). By contrast, a low-Reynolds-number external flow can only exert a significant influence if

$$\mathcal{U} \gtrsim Da^{-1} , \tag{6.19}$$

which, since $Da \ll 1$, requires a much greater external velocity relative to the solidification rate.

6.5 Equations governing the internal evolution of a mushy layer

So far we have considered only the gross features of a mushy layer, which is sufficient to determine the macroscopic envelope of the solid matrix. However, in order to determine the internal structure of the layer, in particular how the solid fraction evolves in space and time, we require a set of differential equations that describe the local distributions of temperature $T(x, t)$, concentration of the interstitial fluid $C(x, t)$ and solid fraction $\phi(x, t)$. Such equations can be derived from considerations of free energy (Hills, Loper & Roberts 1983) or from considerations of the local conservation of heat and solute (Worster 1992a).

Conservation of heat is expressed by

$$\overline{\rho C_p}\left(\frac{\partial T}{\partial t} + \boldsymbol{u} \cdot \nabla T\right) = \nabla \cdot (\overline{k}\nabla T) + \rho_s L \frac{\partial \phi}{\partial t}, \tag{6.20}$$

where the mean conductivity $\overline{k}$ is defined in equation (6.6),

$$\overline{\rho C_p} = \phi \rho_s C_{ps} + (1 - \phi)\rho_l C_{pl} \tag{6.21}$$

and C_{ps} and C_{pl} are the specific heat capacities of the solid and liquid respectively. Equation (6.20) is an advection–diffusion equation forced by the internal release of latent heat as solid grows within the mushy layer.

When the solid phase is pure (C_S is constant), conservation of solute is expressed by

$$(1 - \phi)\frac{\partial C}{\partial t} + \boldsymbol{u} \cdot \nabla C = \nabla \cdot (\overline{D}\nabla C) + (C - C_S)\frac{\partial \phi}{\partial t}, \tag{6.22}$$

where $\overline{D} \simeq (1-\phi)D$. This is an advection–diffusion equation for solute forced by internal release of solute into the interstices as the solid phase grows. Advection–diffusion equations in porous media are slightly modified from their counterparts in a pure phase owing to the fact that the solute is only transported through the liquid interstices (Phillips 1991).

The two equations (6.20) and (6.22) are coupled by the liquidus constraint (6.1), and this coupling is sufficient to determine the solid fraction ϕ.

6.6 The mush–liquid interface

Arguably the most difficult aspect of modelling mushy layers is to determine appropriate equations to describe the interface between a mushy region and a fully liquid region. Some approaches to the modelling of mushy regions (especially numerical modelling) utilize equations that blend smoothly from the mushy regions into the liquid regions, in which case there is no need for

an explicit treatment of the interfaces (see the review by Beckermann & Wang 1995). However, there are some advantages in treating the regions separately, particularly that the equations in each region are then simpler and more amenable to analytic solution from which we can gain physical intuition. One is, however, then left with the problem of matching the solutions across the interface between the regions. The interface itself is hard to define. One can imagine it as the envelope (suitably smoothed) of the solid matrix. On the other hand, since the mushy layer is described by equations that govern properties averaged over the scale of interstitial pores, the interface is perhaps better thought of as a region of thickness comparable to the pore scale. Interfacial conditions are then expressed as jump conditions across the interfacial region. Once one appreciates that the interface physically has finite extent, it is apparent that even continuity of the dependent variables cannot be taken for granted but must either be deduced in some way or assumed and the consequences of those assumptions explored.

Two conditions follow immediately from the conservation equations (6.20) and (6.22) by integrating them across the interface and employing the divergence theorem. They are

$$\rho_s L \phi V_n = \bar{k} \boldsymbol{n} \cdot \nabla T|_m - k_l \boldsymbol{n} \cdot \nabla T|_l \tag{6.23}$$

and

$$(C - C_S)\phi V_n = (1 - \phi) D \mathbf{n} \cdot \nabla C|_m - D \boldsymbol{n} \cdot \nabla C|_l. \tag{6.24}$$

These express conservation of heat and solute across the interface and they reduce to the Stefan condition (4.5b) and the interfacial solute-conservation equation (4.3b) at a solid–liquid interface when $\phi = 1$. A third condition is required at mush–liquid interfaces that are solidifying (but not at those that are melting). A weak condition that suggests itself from considerations of the relief of supercooling (§ 6.1) is that

$$\boldsymbol{n} \cdot \nabla T|_l \geqslant \boldsymbol{n} \cdot \nabla T_L(C)|_l \tag{6.25}$$

so that the liquid is not supercooled adjacent to the interface.

On the other hand, the conservation relationships (6.23) and (6.24) can be combined to show, when $C_S = 0$, that

$$\boldsymbol{n} \cdot \nabla T_L(C)|_l - \boldsymbol{n} \cdot \nabla T|_l = \left(\frac{\rho_s L V_n}{k_l} + \frac{mC V_n}{D} - \frac{k_s}{k_l} \boldsymbol{n} \cdot \nabla T|_m \right) \phi$$

$$= \left(\frac{mC V_n}{D} - \boldsymbol{n} \cdot \nabla T|_l \right) \phi + \left(\boldsymbol{n} \cdot \nabla T|_m - \boldsymbol{n} \cdot \nabla T|_l \right) (1 - \phi). \tag{6.26}$$

The right-hand side is positive once mCV_n/D is greater than $O(\boldsymbol{n} \cdot \nabla T)$, i.e. when the morphological number is significantly greater than its critical value. Then (6.25) and (6.26) combine to show that the inequality (6.25) is in fact an equality and, further, that $\phi = 0$ at the interface.[1]

The three thermodynamic interfacial conditions that apply to a solidifying mush–liquid interface under sufficiently supercritical conditions are therefore

$$\phi = 0, \qquad \boldsymbol{n} \cdot \nabla T|_m = \boldsymbol{n} \cdot \nabla T|_l = \boldsymbol{n} \cdot \nabla T_L(C)|_l . \qquad (6.27a\text{–}c)$$

The fluid-mechanical conditions at a mush–liquid interface are those that apply at the boundary between a porous medium and a viscous fluid region. Only one condition is straightforward, namely that the normal mass flux is continuous, which follows directly from the continuity equation. Two other conditions are related to the transfer of stress between the two media. The difficulty is in knowing how much stress is accommodated by the solid phase of the porous medium. It is usually assumed, for example, that the solid phase absorbs all the deviatoric normal stress exerted by the fluid region, leaving the pressure field continuous between the media.

These two conditions, of normal mass flux and continuity of pressure, are sufficient to determine the flow in the mushy layer, governed by Darcy's equation. The flow in the viscous liquid region requires an additional boundary condition, determined by consideration of the tangential stresses. Where the external liquid makes contact with the solid phase of the mushy layer, its velocity is zero. Where it makes contact with the liquid phase, its velocity is continuous with the *interstitial* velocity. The adjustment from these mixed boundary conditions to a region where the external flow no longer feels the effects of individual crystals takes place on the scale of the pores of the underlying porous medium. Considerations such as these suggest that an appropriate boundary condition on the external flow is

$$\boldsymbol{t} \cdot \boldsymbol{u}_l - \boldsymbol{t} \cdot \boldsymbol{u}_m = \lambda \sqrt{\Pi} \mathscr{S}, \qquad (6.28)$$

where $\mathscr{S} = (\boldsymbol{n} \cdot \nabla)(\boldsymbol{t} \cdot \boldsymbol{u}_l)$ is the local shear rate, $\boldsymbol{t}$ is a unit tangent vector and λ is a constant parameter (Beavers & Joseph 1967). Note that for many external flows u_l is much larger than both u_m and $\sqrt{\Pi} \mathscr{S}$ so that the boundary condition (6.28) can often be approximated by the more familiar no-slip condition.

---

[1] Imposing $\phi = 0$ as a boundary condition *a priori* implies (6.27b, c) given the conservation relations (6.23) and (6.24) and the condition of local equilibrium in the interior of the mushy layer (6.1). However, it can lead to unphysical solutions (with $\phi < 0$ in the interior of the mushy layer) under weakly supercritical conditions when morphological instability precedes the occurrence of constitutional supercooling (Worster 1986).

$$\theta \to \theta_\infty, \qquad \Theta \to 0, \qquad \boldsymbol{u} \to (\mathcal{U}, 0) \qquad (z \to \infty)$$

$$\frac{\partial \theta}{\partial t} + \boldsymbol{u} \cdot \nabla\theta = \nabla^2\theta$$

$$\frac{\partial \Theta}{\partial t} + \boldsymbol{u} \cdot \nabla\Theta = \epsilon\nabla^2\Theta \qquad\qquad \text{Liquid}$$

$$\frac{1}{Pr}\left(\frac{\partial \boldsymbol{u}}{\partial t} + \boldsymbol{u} \cdot \nabla\boldsymbol{u}\right) = \nabla^2\boldsymbol{u} + R_m Da^{-1}\left(\Theta\hat{\boldsymbol{k}} - R_\rho\theta\hat{\boldsymbol{k}} - \nabla p\right)$$

$$[\boldsymbol{u}] = \lambda\, Da\, \mathcal{S}t \qquad\qquad \text{Interface}$$

$$[\boldsymbol{p}] = [\theta] = [\Theta] = [\boldsymbol{n}\cdot\nabla\theta] = [\boldsymbol{n}\cdot\nabla\Theta] = 0$$

$$\phi = 0$$

Mushy layer

$$\frac{\partial \theta}{\partial t} + \boldsymbol{u}\cdot\nabla\theta = \nabla^2\theta + S\frac{\partial \phi}{\partial t}$$

$$(1-\phi)\frac{\partial \Theta}{\partial t} + \boldsymbol{u}\cdot\nabla\Theta = \epsilon\nabla\cdot[(1-\phi)\nabla\Theta] + (\Theta - \mathcal{C})\frac{\partial \phi}{\partial t}$$

$$\boldsymbol{u} = -R_m\left(\Theta\hat{\boldsymbol{k}} - R_\rho\theta\hat{\boldsymbol{k}} - \nabla p\right)$$

$$\theta = \Theta$$

$$\theta = -1, \qquad\qquad \boldsymbol{n}\cdot\boldsymbol{u} = 0 \qquad\qquad (z = 0)$$

Figure 12. The equations and boundary conditions governing flow and solidification in a mushy layer growing from a binary melt. The boundary $z = 0$ is either the cooled boundary of a mould of fixed temperature T_B or the eutectic front with $T_B = T_E$. Lengths are scaled with κ/V, times with V^2/κ and velocities with V, where V is the rate of solidification. The dimensionless dependent variables are the velocity $\boldsymbol{u}$, pressure p, temperature $\theta = (T - T_L(C_0))/(T_L(C_0) - T_B)$ and concentration $\Theta = (C - C_0)/(C_0 - C_B)$. The importance of each of the dimensionless parameters $S, \mathcal{C}, \theta_\infty, \mathcal{U}, \epsilon, \mathcal{A}, R_m, R_\rho$ and Da is discussed in the text.

7 Solidification and convection in mushy layers

The equations and boundary conditions discussed in the previous section are summarized in dimensionless form for a solidifying system in figure 12, with the dimensionless variables defined in the caption. The equations have been simplified by taking the thermal properties of the liquid and solid phases to be equal. There are, nevertheless, a large number of dimensionless parameters
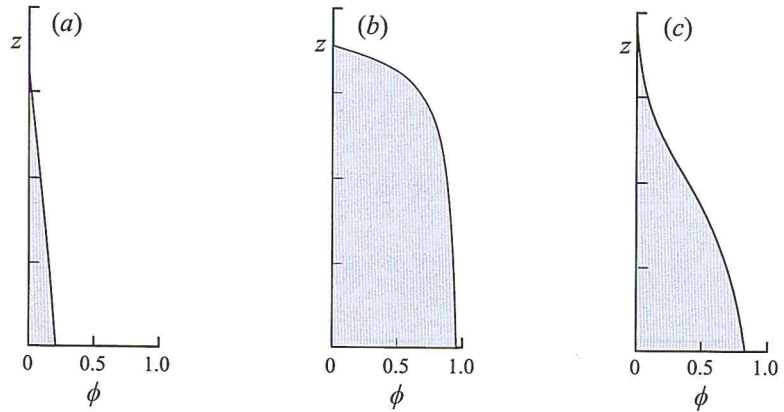
M. G. Worster

Figure 13. Solid-fraction profiles in a mushy layer when there is no convection:
(a) $\mathscr{C} = 4, \theta_\infty = 1$; (b) $\mathscr{C} = 0.05, \theta_\infty = 1$; (c) $\mathscr{C} = 0.2, \theta_\infty = 0.02$. In all cases $S = 1$
and $\epsilon = 0$.

controlling the dynamical behaviour of the system. In this section we shall
simply describe the importance of the different parameters and some of the
phenomena that have been calculated using these equations.

Three parameters govern the structure of the mushy layer in the absence
of flow. As the thickness of the mushy layer is controlled by thermal bal-
ances, it decreases as the far-field temperature θ_∞ increases and as the Stefan
number S increases, since these increase the heat flux from the melt and the
latent heat release respectively. The release of latent heat is further modified
by the concentration ratio $\mathscr{C}$ since this, as we have seen, controls the mean
solid fraction. When $\mathscr{C}$ is large, the solid fraction is inversely proportional to
$\mathscr{C}$ and the total latent heat release is therefore proportional to $S/\mathscr{C}$. This can
be seen from (6.4) to (6.7) which show that the thickness of a mushy layer
$h \propto \sqrt{(\mathscr{C}/S)\kappa t}$ in contrast to a pure solid whose thickness $h \propto \sqrt{(1/S)\kappa t}$
(see 2.11). The internal distribution of solid fraction is controlled predom-
inantly by $\mathscr{C}$, as illustrated in figure 13, so this is the most significant
parameter determining the variation of the permeability of the layer to fluid
flow.

The diffusivity ratio ϵ plays a minor role when there is no flow and can
be set to zero in such cases. However, while this is a regular perturbation in
the mushy layer, it is a singular perturbation of the equations in the liquid
region. There is a compositional boundary layer in the liquid adjacent to the
mush–liquid interface of width $\delta_c \sim \epsilon$ in the case of constant solidification
rate or of width $\delta_c \sim \epsilon^{1/2}$ in the case of solidification from a cooled boundary
with growth proportional to $t^{1/2}$. This boundary layer can often be resolved

experimentally and can itself become unstable in a gravitational field to produce compositional convection.

We have seen how flow in the mushy layer can be generated by an imposed flow $\mathcal{U}$. However, a more common mechanism for fluid flow during solidification is natural, buoyancy-driven convection. Within the mushy layer, this is governed principally by the Rayleigh number

$$R_m = \frac{\beta \Delta C g \Pi_0 h}{\kappa \nu} \tag{7.1}$$

which is a porous-medium Rayleigh number for compositional convection, where $\beta = \rho^{-1} \partial \rho / \partial C$, $\Delta C = C_0 - C_B$ is the change in interstitial concentration across the layer, and Π_0 is a representative value of the permeability. We see from figure 12 that, since the dimensionless temperature and concentration are equal ($\theta = \Theta$) in the mushy layer, there is effectively only single-component convection there with an effective Rayleigh number $R_m(1 - R_\rho)$ where

$$R_\rho = \frac{\alpha \Delta T}{\beta \Delta C} = \frac{\alpha m}{\beta} \tag{7.2}$$

is the buoyancy ratio in which $\Delta T = T_L(C_0) - T_B$ and α is the thermal expansion coefficient. Note that, typically, $R_\rho < 1$ so that convection in the mushy layer is dictated by the solute field.

In the liquid region, the temperature and solute fields are uncoupled and convection is better described by the independent Rayleigh numbers

$$R_C \equiv R_m Da^{-1} \equiv \frac{\beta \Delta C g h^3}{\kappa \nu} \tag{7.3}$$

for solutal convection and

$$R_T \equiv -R_m Da^{-1} R_\rho \equiv -\frac{\alpha \Delta T g h^3}{\kappa \nu} \tag{7.4}$$

for thermal convection, as can be seen from the equations in figure 12. Many interesting double-diffusive effects (Turner 1979) can occur in the melt during solidification (Huppert 1990) owing to the independence of R_T and R_C.

7.1 Convective regimes

The possible states of natural convection in a solidifying alloy are summarized in figure 14 for the cases where solidification is effected by cooling a mould either from an upper or a lower horizontal boundary. Other modes of convection that occur when there is cooling through sidewalls are not discussed here (but see Huppert 1990). Note that the equations in figure 12

	Cooled from below $R_T < 0$	Cooled from above $R_T > 0$
$C_0 < C_E$ Heavy fluid released	3. $R_C < 0, R_m < 0$ Mushy layer No convection	5. $R_C > 0, R_m > 0$ Mushy layer Compositional convection in liquid and mushy regions Themal convection in liquid
$C_0 = 0, C_E, 100$ Neutrally buoyant residual	1. $R_C = 0$ No mushy layer No convection	2. $R_C = 0$ No mushy layer Thermal convection
$C_0 > C_E$ Light fluid released	6. $R_C > 0, R_m > 0$ Mushy layer Compositional convection in mushy region Double-diffusive convection in liquid	4. $R_C < 0, R_m < 0$ Mushy layer Themal convection in liquid

Figure 14. The different convective regimes that can occur during solidification of a binary alloy at a cooled, horizontal boundary. The numbered cases 1–6 are discussed in turn in the text.

and the definitions of Rayleigh numbers therein are written for the case where gravity acts towards the cooled boundary, i.e. for when cooling is through the lower boundary. Cases in which the upper boundary of the mould is cooled are described by changing the sign of the Rayleigh number. The various boxes in figure 14 are now described in turn.

Case 1. If the melt is pure ($C_0 = 0$ or $C_0 = 100$) or if it has exactly the eutectic concentration ($C_0 = C_E$) then the solid formed has the same composition as the melt, there is no rejected solute and the solute field plays no role in the solidification or convection. If, in addition, the mould is cooled from below then the melt is statically stable to thermal convection.[1] There is therefore no convection, and solidification proceeds at a planar interface as described in §2.2.

Case 2. In this case there is again no solute rejection, no mushy layer can form (provided the melt is not initially supercooled) and there is no compositional convection. Since the mould is cooled from above, the melt is unstable to thermal convection and its solidification is described in §3.2.

Case 3. If the melt is neither pure nor of eutectic composition then solute is rejected during solidification and, in the general case, a mushy layer will form. When the melt has an initial composition less than eutectic (where C measures the component that causes the density of the melt to increase) then the residual melt is denser than the initial melt. The liquid is therefore stable

---

[1] Note that in the special case of pure water there is density maximum at 4°C so there is thermal convection when ice is formed by freezing pure water from below.

to compositional convection when the mould is cooled from below. In this case the thermal field is also stable so there is no convection and the mushy layer grows as described in §6.2.

Case 4. The solute field is also stable in the case that the melt has an initial composition that is greater than eutectic (so that the residual melt is buoyant) and the mould is cooled from above. The cooling drives convection in the liquid region only (the mushy layer remains stagnant) and solidification proceeds similarly to that in case 2 but with the latent heat release now distributed throughout the mushy layer (Kerr *et al.* 1990*a*). There are some very interesting additional effects in this case associated with supercooling at the mush–liquid interface, which will be described in the context of lava lakes in the next section.

Case 5. When the mould is cooled from above and the residual melt is denser than the initial melt then thermal and compositional convection act in concert. Thermal convection in the liquid region is augmented slightly by the solutal buoyancy from the compositional boundary layer near the mush–liquid interface but otherwise proceeds similarly to that in cases 2 and 4. The new effect here is that the interstitial liquid in the mushy layer is now also statically unstable. Convection can be driven from the interior of the mushy layer leading to interesting modifications of its microstructure, as described below in general and also in the context of the formation of sea ice.

Case 6. Directional casting of high-performance turbine blades (for example) is executed by withdrawing a mould vertically downwards from a hot furnace, so that the mould is cooled from below and the thermal field is convectively stable. If the residual melt is less dense, however, then compositional convection can occur in both the liquid and mushy regions. The convection in the mushy layer is similar to that in case 5 with the effective Rayleigh number simply being $R_m(1 - R_\rho)$ rather than $R_m(1 + R_\rho)$. The stable thermal field in the liquid region can, however, modify the compositional convection there and cause the formation of double-diffusive 'fingers' (Turner 1979; Chen & Chen 1991; and see Chapter 6).

7.2 Convection within a mushy layer

The last two cases described above both involve convection of the interstitial liquid within the mushy layer (reviewed by Worster 1997). To analyse such convection in detail it is necessary to solve the full set of equations displayed in figure 12. However, we can make a preliminary estimate of the conditions under which internal convection will occur by analysing the following much-reduced model.

A major simplification is obtained by arbitrarily ignoring the fact that the mush–liquid interface is a free boundary and fixing it at the dimensionless position $z = 1$. The remaining simplifications follow from asymptotic limits of the governing equations. In particular we take $\epsilon \to 0$ and $Da \to 0$.

If $\mathscr{C} \gg 1$ then $\phi \ll 1$ and the solute-conservation equation is approximately

$$\frac{\partial \theta}{\partial t} + \boldsymbol{u} \cdot \nabla \theta = -\mathscr{C} \frac{\partial \phi}{\partial t} \tag{7.5}$$

whence the heat-conservation equation becomes

$$\Omega \left(\frac{\partial \theta}{\partial t} + \boldsymbol{u} \cdot \nabla \theta \right) = \nabla^2 \theta, \tag{7.6}$$

where $\Omega = 1 + S/\mathscr{C}$ and we have taken $S \gg 1$ with $S/\mathscr{C} = O(1)$. The heat equation is thus decoupled from the solute equation, as derived by Emms & Fowler (1994). Since $\phi \ll 1$ throughout the mushy layer, the permeability is approximately constant. If we also assume that $R_\rho \ll 1$ then Darcy's equation becomes

$$\boldsymbol{u} = -R_m (\nabla p + \theta \boldsymbol{k}), \tag{7.7}$$

where $\boldsymbol{k}$ is a unit vector in the z-direction. The relevant boundary conditions given the limits stated above are

$$\theta = -1, \quad \boldsymbol{n} \cdot \boldsymbol{u} = 0 \quad (z = 0), \qquad \theta = p = 0 \quad (z = 1). \tag{7.8}$$

These equations are mathematically identical to the equations for convection in a passive porous medium. By writing $\Omega \boldsymbol{u} = \boldsymbol{v}$ and $t = \Omega \tau$, so that

$$\frac{\partial \theta}{\partial \tau} + \boldsymbol{u} \cdot \nabla \theta = \nabla^2 \theta \quad \text{and} \quad \boldsymbol{v} = -(R_M \Omega)(\nabla p + \theta \boldsymbol{k}), \tag{7.9}$$

we see that the Rayleigh number is simply modified by the factor Ω. The stability of this system was analysed by Lapwood (1948) who showed that convection begins once

$$\Omega R_m > \Omega R_{\text{crit}} \simeq 27.1. \tag{7.10}$$

More generally, the critical Rayleigh number for linear convective instability $R_{\text{crit}} = R_{\text{crit}}(S, \mathscr{C}, \theta_\infty, \epsilon, R_\rho, Da)$. Some of this parameter space has been explored (Worster 1992b; Chen, Lu & Yang 1994; Emms & Fowler 1994) and it has been shown that, over a large range of parameters, provided one rescales the Rayleigh number in terms of the mean permeability of the layer and its undisturbed depth, the critical Rayleigh number R_{crit} is, within a factor of 2, equal to about 10. This much-reduced model embodies the interesting feature that systems with large Stefan numbers (or small $\mathscr{C}$) are
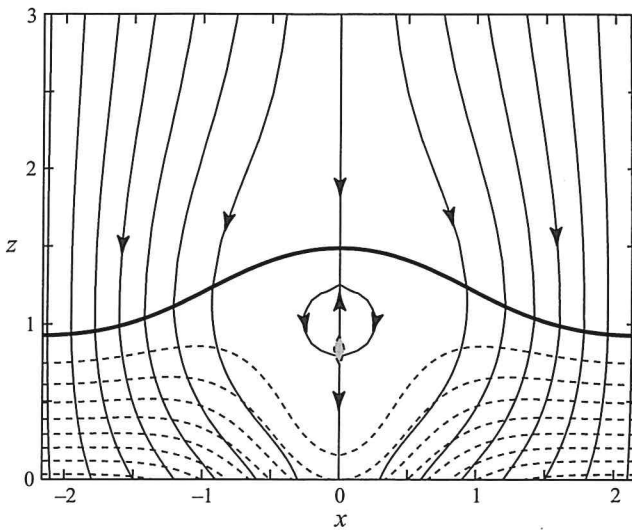
Figure 15. The streamlines (thin solid lines with arrows) and contours of solid fraction (dashed lines) in a steadily solidifying and convecting mushy layer below a liquid melt. Streamlines are shown in a frame of reference moving with the phase boundaries. The mush–liquid interface (thick solid line) is deformed upwards where the flow towards the mushy layer (relative to the interface) is weaker. Below the upwardly deflected interface the solid fraction is reduced and has become negative in the small shaded region near the bottom of the recirculating region interior to the mushy layer. It is anticipated that the shaded region, which must be liquid, develops into a chimney (figure 16) as the amplitude of convection increases.

more prone to convection. The reason for this highlights the fact that the mushy layer is a *reactive* porous medium. Although the driving buoyancy results from the solute field, the dissipation of that buoyancy is mediated by the thermal field as follows. When a parcel of interstitial fluid rises, it approaches thermal equilibrium with its surroundings by diffusion of heat but does not similarly exchange solute with its new surroundings. Rather, since an approach to thermal equilibrium without any phase change would leave the interstitial liquid undersaturated (above the liquidus), equilibrium is restored by dissolution of the solid matrix. This causes the interstitial liquid to become more dense (in case 6), and thus dissipates the buoyancy. Systems with large Stefan number can dissolve less of the solid matrix for a given thermal perturbation and are therefore more unstable.

The dissolution just described is manifest in equation (7.5), which shows that the rate of solidification ($\partial \phi / \partial t$) is reduced where the flow has a component parallel to the local temperature gradient, i.e. where the interstitial liquid flows from cooler to warmer regions of the mushy layer. This corresponds to downflow in case 5 and upflow in case 6 above.
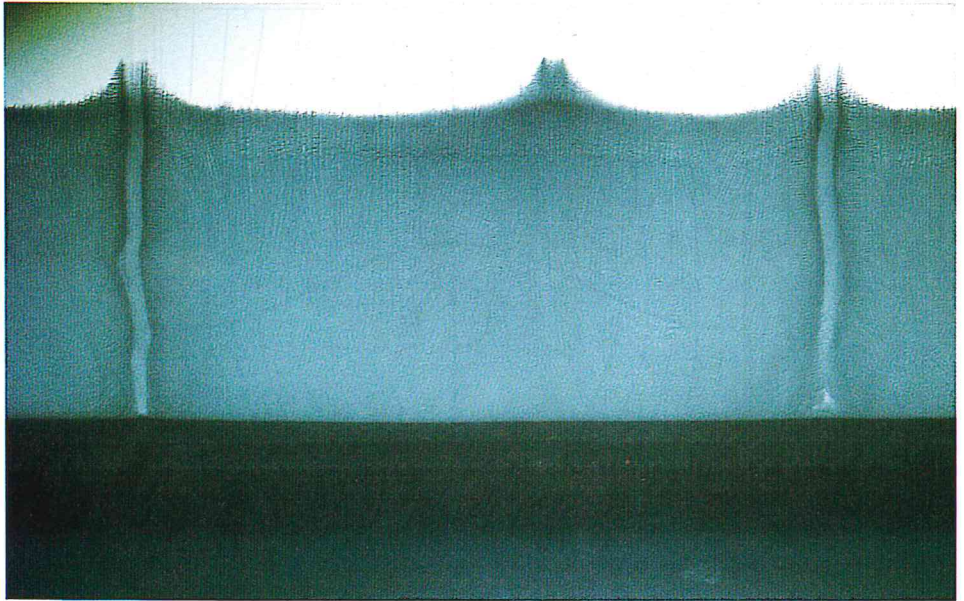
Figure 16. Photograph of a mushy layer of ammonium-chloride crystals grown from aqueous solution showing sections through two complete chimneys and the vent of a third. The black region at the bottom of the photograph is eutectic solid and shows that the interface of this region with the mushy layer is quite planar. The mush–liquid interface, by contrast, is deflected upwards at the sites of chimneys to form a volcano-like vent. A plume of depleted fluid issues from each chimney into the overlying melt. This picture turned upside down is similar to what is seen in sea ice, in which case dense brine drains from the chimneys, which are known as brine channels.

Such dissolution (or reduced solidification) increases with the amplitude of the convective motion until the solid fraction becomes equal to zero at some point in the mushy layer. Recent numerical calculations (Schulze & Worster 1999) have shown that this can occur in the interior of the layer, as shown in figure 15. At even larger convective amplitudes the region of zero solid fraction can form a narrow cylindrical conduit, or *chimney* through which most of the outflow from the mushy layer is channelled (see figure 16). Convection through fully developed chimneys, particularly the theoretical determination of the location of the chimney wall, remains a topic of current research.

7.3 The early evolution of sea ice

Many of the fundamental ideas presented in this chapter are illustrated in two case studies with which I shall conclude. The first is a study of the

growth of sea ice on the surface of the polar oceans. The Arctic ocean is covered with a layer of ice with a mean thickness of about 3 m. Owing to wind stresses, the ice is in a very dynamic state, being continually fractured to expose sea water to the atmosphere. The exposed water in these cracks, or *leads*, quickly freezes over and the ice begins to grow downwards, reaching a thickness of about 1 m in the first winter season if left undeformed. It is in the first 24 hours or so of growth, while the ice is less than about 10 cm thick, that the most significant heat transfer takes place between the ocean and the atmosphere, and these episodes of lead formation and early ice growth account for about half the total heat budget. It is therefore very important to understand the processes controlling the dynamics of this early growth.

Since sea water is a mixture of water and dissolved salts (an alloy in the terminology adopted here), sea ice is a mushy layer comprising a matrix of ice crystals and interstitial brine. Because brine is denser than fresh water, growing sea ice is an example of case 5 from § 7.1. We can therefore anticipate that, under appropriate conditions, the interstitial brine will convect out of the layer of sea ice and contribute to the convective state of the underlying ocean.

A laboratory study of sea ice (Wettlaufer, Worster & Huppert 1997, illustrated and described in figure 17) has shown that there is no measurable brine flux from the mushy layer until it has exceeded a critical thickness h_c that depends upon the applied surface temperature (atmospheric temperature) and initial concentration of the salt solution. Before the critical thickness has been reached, the mushy layer is stagnant and its growth can be described approximately by the model presented in § 6.2, modified slightly by the heat flux from the ocean, as described in § 3.2. An important parameter influencing the remote sensing of sea ice by satellite, using radar, is its solid fraction, which can be readily calculated from the equations presented in section § 6.5, as shown in figure 13.

The critical thickness h_c can in principal be determined from the stability analysis described in the previous section. However, a problem with this is that the permeability of the mushy layer is difficult to measure directly. An alternative approach is to notice that equation (7.10) implies that

$$[(C_0 - C_B)h_c]^{-1} \propto \Pi(\phi) \tag{7.11}$$

or that $h_c \Delta C$ is a function only of the solid fraction and material parameters. A plot of the data from many experiments starting with different initial concentrations and having different surface temperatures (figure 18) shows
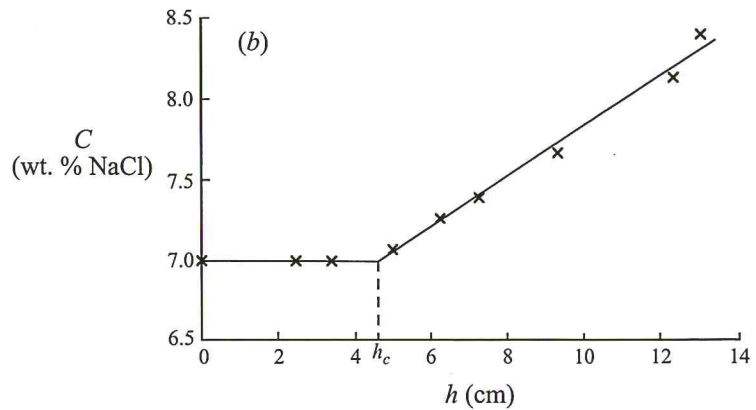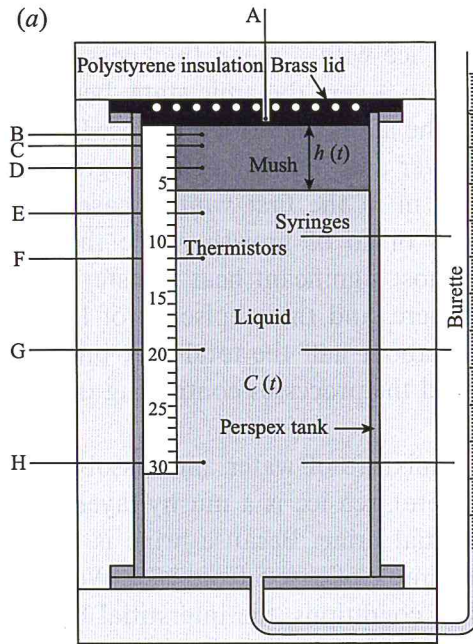
Figure 17. (a) Experimental apparatus used by Wettlaufer et al. (1997) to study the early growth of sea ice. A mushy layer of ice crystals was grown from aqueous solutions of NaCl by cooling the upper boundary of the apparatus. Temperatures were recorded by thermistors A–H and samples of liquid were withdrawn periodically using syringes in order to measure the evolving concentration $C(t)$ of the liquid region. These data are plotted against the thickness of the mushy layer $h(t)$ in (b). Initially all the brine rejected by the growing ice crystals remains within the interstices of the mushy layer but it subsequently drains once the thickness of the layer has exceeded a critical value h_c.

$$h_c(C_0 - C_B)$$

Strong compositional
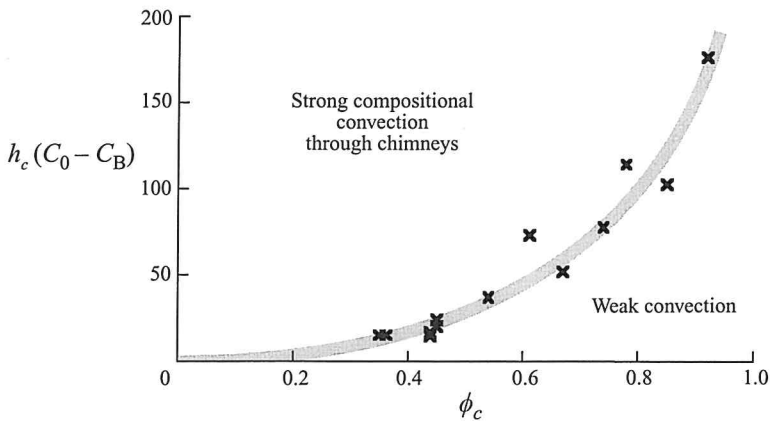convection
through chimneys

Weak convection

ϕ_c

Figure 18. The critical conditions for brine drainage from sea ice.

that equation (7.11) gives a good collapse of all the data onto a single curve. This curve gives reasonable values for the permeability as a function of the solid fraction (increasing rapidly as the solid fraction approaches zero). In particular, if R_{crit} is taken to be equal to 10 then the permeability of typical young sea ice (having a solid fraction between 0.6 and 0.8) is predicted to be about 10^{-10} m^2, which is reasonable given the scale of observed microstructures (platelets approximately 1 mm thick separated by about 0.1 mm).

Once the critical thickness is exceeded, brine begins to drain from the sea ice and does so via narrow *brine channels*, which are the chimneys described in the previous section. Brine channels are home to a host of organisms which feed on nutrients from the sea water that flushes through them. Theoretical and experimental studies of convection in mushy layers suggest that the flow permeates the sea ice surrounding brine channels, originating from the underlying ocean and draining through the channels. During its passage through the porous sea ice, continued solidification of ice enriches the remaining liquid both in salt and in nutrients. Brine channels are therefore rich harvesting grounds in addition, no doubt, to being relatively safe havens from predators.

The brine draining from sea ice raises the density of the oceanic mixed layer beneath it and therefore contributes to its deepening during the winter months. The seasonal dynamics of the mixed layer is a significant factor affecting climate, so the small-scale processes occurring within the mushy layer that is sea ice may have important global consequences.

Figure 19. Photograph of a lava lake in Hawaii.

7.4 Mineral segregation in lava lakes

Nature provides many examples of large-scale casting processes. The largest is the growth of the inner core of the Earth (see Chapter 9), while numerous smaller examples are given by the solidification of magmas and lavas to form igneous rocks. One relatively uncomplicated example is the solidification of lava that has ponded within the crater of a volcano to form a *lava lake* (figure 19). The lake is cooled predominantly by contact with the atmosphere above it. We can ignore the relatively small heat transfer to the rock beneath and to the sides of it, which complicate considerations of solidification in intrusive magmas (dykes and sills). The lava lake therefore fits well the ideal case 4 of § 7.1, the first minerals to solidify typically being the densest.

Examination of solidified lava lakes shows that, in addition to crystals growing adjacent to the cooled top to form a crust, a significant proportion of the crystallization occurs in its interior. Similar behaviour occurs in metallic castings, in which there is also a textural division between *columnar* crystals formed adjacent to the boundaries of a mould, being elongated and aligned normal to the boundaries, and *equiaxed* crystals that grow in the interior. The marginal crystals in a lava lake or magma chamber and the
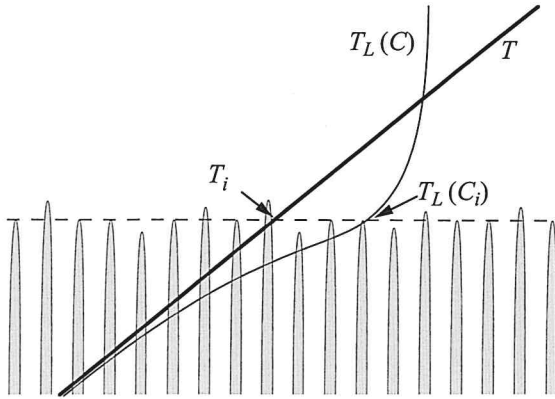
Figure 20. Schematic diagram of the interfacial region of a mushy layer showing the mean temperature T and mean liquidus temperature $T_L(C)$. The horizontal dashed line shows the position of maximum undercooling $T_L(C) - T$. Dendrites further into the liquid than this grow slower than the mean and are caught up by the others. Those that recede from this position grow slower and cease to contribute to the interfacial conditions. This reasoning suggests that the mush–liquid interface is located where $\boldsymbol{n}\cdot\nabla[T_l(C) - T] = 0$, which is mathematically identical to the condition of marginal equilibrium. In systems with slow kinetics the interfacial undercooling is significant and, coupled with convection of the melt, can have large-scale effects in a casting.

columnar crystals in a metallic casting form the matrices of mushy layers during solidification.

There is a problem in describing how the interior crystals can grow given the theory of solidification presented so far. The assumptions of internal equilibrium (6.1) and, more importantly, of marginal equilibrium (6.25) ensure that the liquid region can never be cooled below its liquidus. Crystals cannot grow in suspension in such a liquid and solidification only occurs within the mushy layer.

However, as discussed in §2.3, the surface of a growing crystal is at a temperature below the freezing temperature of the melt. If the local normal growth of each crystal within a mushy layer obeys an equation of the form of (2.15) then the solid fraction must evolve according to an equation of the form

$$\frac{\partial \phi}{\partial t} = \mathscr{A}\mathscr{G}[T_L(C) - T], \qquad (7.12)$$

where $\mathscr{A}$ is the specific surface area of the internal phase boundaries. Morphological instabilities within the mushy layer serve to increase $\mathscr{A}$, and it is clear from (7.12) that if $\mathscr{A}\mathscr{G}$ is large then $T \simeq T_L(C)$, which is
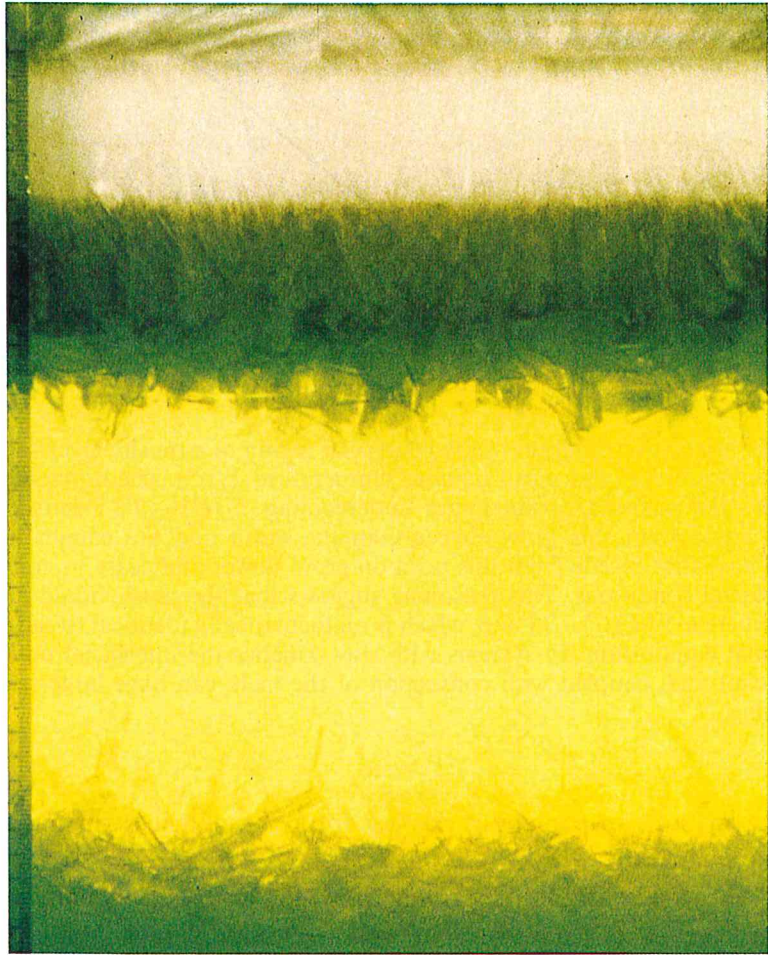
Figure 21. Photograph of an experiment (Kerr *et al.* 1990*b*) in which an aqueous solution of sodium sulphate was solidified by cooling it at the top boundary of a rectangular mould. At the top of the mould is a white region of eutectic solid above a mushy layer of hydrated sodium-sulphate crystals $Na_2SO_4.10H_2O$. Supercooling of the solution, as explained in the text, allows further crystallization of equiaxed crystals at the floor of the mould.

the condition of local, internal equilibrium (6.1). However, near the interface with the liquid region the morphological instabilities on the primary dendrites leading to side branches are not fully developed and one can anticipate that higher degrees of supercooling prevail in the interfacial region, as sketched in figure 20. It is clear, by differentiating the right-hand side of (7.12) that the maximum rate at which the mush–liquid interface can advance occurs when the tips of the primary dendrites sit where the undercooling is largest,
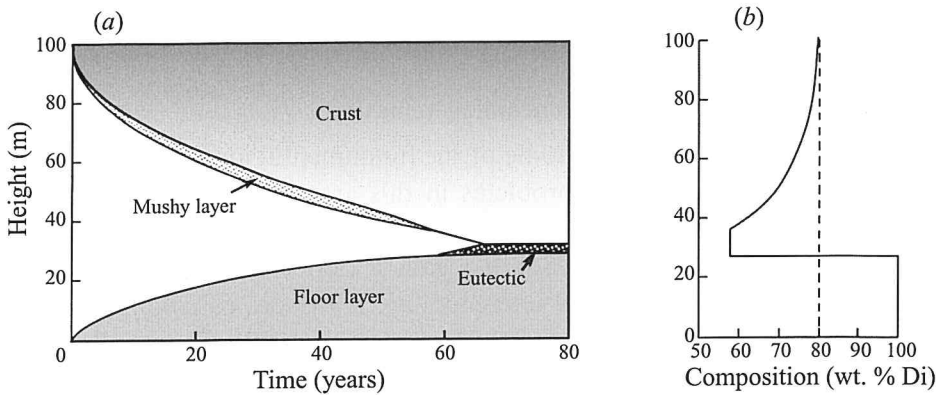
Figure 22. (a) The predicted evolution of a hypothetical lava lake composed of Diopside (Di) and Anorthite (An) (Worster *et al.* 1993). A eutectic crust and underlying mushy layer grow downwards from the upper surface of the lake, while further crystals grow in the interior and settle to the floor. The composition of the melt evolves as it is depleted of the minerals forming the interior crystals. (b) The predicted distribution of minerals in the lava lake once it is completely solidified.

i.e. where

$$\boldsymbol{n} \cdot \nabla\left[T_L(C) - T\right] = 0. \tag{7.13}$$

This provides further justification of the condition (6.27c) derived previously from considerations of marginal equilibrium and applies regardless of the degree of interfacial supercooling. What is apparent in figure 20 is that $T_i \neq T_L(C_i)$. In consequence, the solid fraction is non-zero at the interface.

All this has negligible influence on the growth of the mushy layer. However, if the liquid region is flowing then supercooled liquid can be swept from the neighbourhood of the interface into the bulk of the region. The whole liquid region can thereby become supercooled, allowing additional solidification of crystals from any suitable nucleation sites within that region (figure 21, Kerr *et al.* 1990b). In the case of lava lakes, there are numerous small crystals (phenocrysts) that can act as nucleation sites for such secondary crystallization. In metal castings it is common to add small particles to the melt to promote such growth in cases where this is desired.

There is a further twist to the tale in that as the suspended crystals grow and settle they leave the melt depleted of the high-melting point minerals that form them. The composition of the melt thus evolves and its time history is frozen into the mushy layer as it grows downwards from the surface of the lake. The bulk composition of the frozen lake, though the lava was initially uniform, has a continuous stratification in its upper regions and changes

abruptly where the mushy layer meets the accumulated equiaxed crystals (figure 22).

8 Concluding remarks

In this chapter we have visited some of the fundamental ideas involved in the solidification of fluids. Many problems in this area derive from metallurgy, and students can gain a fuller background from the texts by Flemings (1974) and Kurz & Fisher (1986). To gain a better understanding of the mathematical techniques, useful references are Alexiades & Solomon (1993), Carslaw & Jaeger (1959), Crank (1984) and Hill (1987). There is a broad range of excellent reviews covering many of the modern developments in the subject in the *Handbook of Crystal Growth* edited by Hurle (1993).

An understanding of the solidification of fluid melts is becoming increasingly important as we try to develop better ways to process more exotic materials. It is similarly important in many geophysical contexts. There are many unsolved problems related to solidification from atomic to planetary scales and the fluid dynamist can make significant contributions in predicting behaviour and developing controlling strategies for the future.

Acknowledgements

References

ALEXIADES, V. & SOLOMON, A. D. 1993 *Mathematical Modeling of Melting and Freezing Processes.* Hemisphere.

BATCHELOR, G. K. 1967 *An Introduction to Fluid Dynamics.* Cambridge University Press.

BATCHELOR, G. K. 1974 Transport properties of two-phase materials with random structure. *Ann. Rev. Fluid Mech.* **6**, 227–255.

BEAVERS, G. S. & JOSEPH, D. D. 1967 Boundary conditions at a naturally permeable wall. *J. Fluid Mech.* **30**, 197–207.

BECKERMANN, C. & WANG, C. Y. 1995 Transport phenomena in alloy solidification. In *Annual Review of Heat Transfer VI* (ed. C. L. Tien), pp. 115–198, Begell House.

BRATTKUS, K. & DAVIS, S. H. 1988 Flow-induced morphological instabilities: stagnation-point flows. *J. Cryst. Growth* **89**, 423–427.

BÜHLER, L. & DAVIS, S. H. 1998 Flow induced changes of the morphological stability in directional solidification: localized morphologies. *J. Cryst. Growth* **186**, 629–647.

CARSLAW, H. S. & JAEGER, J. C. 1959 *Conduction of Heat in Solids*. Cambridge University Press.

CHEN, F. & CHEN, C. F. 1991 Experimental study of directional solidification of aqueous ammonium chloride solution. *J. Fluid Mech.* **227**, 567–586.

CHEN, F., LU, J. W. & YANG, T. L. 1994 Convective instability in ammonium chloride solution directionally solidified from below. *J. Fluid Mech.* **276**, 163–187.

CRANK, J. 1984 *Free- and Moving-Boundary Problems*. Clarendon Press.

DAVIS, S. H. 1990 Hydrodynamic interactions in directional solidification. *J. Fluid Mech.* **212**, 241–262.

EMMS, P. W. & FOWLER, A. C. 1994 Compositional convection in the solidification of binary alloys. *J. Fluid Mech.* **262**, 111–139.

FELTHAM, D. L. & WORSTER, M. G. 1999 Flow induced morphological instability in a mushy layer. *J. Fluid Mech.* **391**, 337–357.

FLEMINGS, M. C. 1974 *Solidification Processing*. McGraw-Hill.

FORTH, S. A. & WHEELER, A. A. 1989 Hydrodynamic and morphological stability of the unidirectional solidification of a freezing binary alloy: a simple model. *J. Fluid Mech.* **202**, 339–366.

GLICKSMAN, M. E., CORIELL, S. R. & McFADDEN, G. B. 1986 Interaction of flows with the crystal–melt interface. *Ann. Rev. Fluid Mech.* **18**, 307–335.

GLICKSMAN, M. E. & MARSH, S. P. 1993 The Dendrite. In *Handbook of Crystal Growth 1, Part B: Transport and Stability* (ed. D. T. J. Hurle). North Holland.

HILL, J. M. 1987 *One-dimensional Stefan Problems: An Introduction*. Longman.

HILLS, R. N., LOPER, D. E. & ROBERTS, P. H. 1983 A thermodynamically consistent model of a mushy zone. *Q. J. Mech. Appl. Math.* **36**, 505–539.

HUPPERT, H. E. 1990 The fluid mechanics of solidification. *J. Fluid Mech.* **212**, 209–240.

HUPPERT, H. E. & WORSTER, M. G. 1985 Dynamic solidification of a binary melt. *Nature* **314**, 703–707.

HUPPERT, H. E. & WORSTER, M. G. 1991 Vigorous motions in magma chambers and lava lakes. In *Chaotic Processes in the Geological Sciences* (ed. D. A. Yuen). Springer.

HURLE, D. T. J. (Ed.) 1993 *Handbook of Crystal Growth. Volume 1: Fundamentals, A: Thermodynamics and Kinetics, B: Transport and Stability*. North Holland.

KERR, R. C., WOODS, A. W., WORSTER, M. G. & HUPPERT, H. E. 1990a Solidification of an alloy cooled from above. Part 1. Equilibrium growth. *J. Fluid Mech.* **216**, 323–342.

KERR, R. C., WOODS, A. W., WORSTER, M. G. & HUPPERT, H. E. 1990b Solidification of an alloy cooled from above. Part 3. Compositional stratification within the solid. *J. Fluid Mech.* **218**, 337–354.

KIRKPATRICK, R. J. 1975 Crystal growth from the melt: a review. *Am. Mineral.* **60**, 798–814.

KURZ, W. & FISHER, D. J. 1986 *Fundamentals of Solidification*. Trans. Tech. Publications.

LANGER, J. S. 1980 Instabilities and pattern formation in crystal growth. *Rev. Mod. Phys.* **52**, 1–28.

LAPWOOD, E. R. 1948 Convection of a fluid in a porous medium. *Proc. Camb. Phil. Soc.* **44**, 508–521.

MULLINS, W. W. & SEKERKA, R. F. 1964 Stability of a planar interface during solidification of a dilute binary alloy. *J. Appl. Phys.* **35**, 444–451.

NIELD, D. A. & BEJAN, A. 1999 *Convection in Porous Media.* Springer.

PHILLIPS, O. M. 1991 *Flow and Reactions in Permeable Rocks.* Cambridge University Press.

SCHULZE, T. P. & DAVIS, S. H. 1995 Shear stabilization of morphological instability during directional solidification. *J. Cryst. Growth* **149**, 253–265.

SCHULZE, T. P. & WORSTER, M. G. 1999 Weak convection, liquid inclusions and the formation of chimneys in mushy layers. *J. Fluid Mech.* **388**, 197–215.

TURNER, J. S. 1979 *Buoyancy Effects in Fluids.* Cambridge University Press.

UMANTSEV, A. R. 1985 Motion of a plane front during crystallization. *Sov. Phys. Crystallogr.* **30**(1), 87–91.

WETTLAUFER, J. S., WORSTER, M. G. & HUPPERT, H. E. 1997 Natural convection during solidification of an alloy from above with application to the evolution of sea ice. *J. Fluid Mech.* **344**, 291–316.

WORSTER, M. G. 1986 Solidification of an alloy from a cooled boundary. *J. Fluid Mech.* **167**, 481–501.

WORSTER, M. G. 1992a The dynamics of mushy layers. In *Interactive Dynamics of Convection of Solidification,* (ed. S. H. Davis, H. E. Huppert, W. Müller & M. G. Worster), NATO ASI ser. E219, pp. 113–138. Kluwer.

WORSTER, M. G. 1992b Instabilities of the liquid and mushy regions during solidification of alloys. *J. Fluid Mech.* **237**, 649–669.

WORSTER, M. G. 1997 Convection in mushy layers. *Ann. Rev. Fluid Mech.* **29**, 91–122.

WORSTER, M. G., HUPPERT, H. E. & SPARKS, R. S. J. 1993 The crystallization of lava lakes. *J. Geophys. Res.* **98** (B9), 15891–15901.

XU, J.-J. 1994 Dendritic growth from a melt in an external flow: uniformly valid asymptotic solution for the steady state. *J. Fluid Mech.* **263**, 227–243.

Institute of Theoretical Geophysics, Department of Applied Mathematics and Theoretical Physics, Silver Street, Cambridge CB3 9EW, UK